AGU PUBLICATIONS

Journal of Advances in Modeling Earth Systems

RESEARCH ARTICLE

10.1002/2017MS000960

Key Points:
- Multiscale modeling of a real-world diurnal cycle is presented for the first time, enabled by the generalized cell perturbation method
- The multiscale simulations exhibited realistic atmospheric features not captured by the mesoscale model such as convective rolls, global intermittency, and intra-hour variability
- Diurnal evolution of turbulence was accurately simulated, with probability density functions of resolved turbulent velocity fluctuations nearly identical to CWEX-13 lidar measurements

Correspondence to:
D. Muñoz-Esparza,
domingom@ucar.edu

Citation:
Muñoz-Esparza, D., J. K. Lundquist, J. A. Sauer, B. Kosović, and R. R. Linn (2017), Coupled mesoscale-LES modeling of a diurnal cycle during the CWEX-13 field campaign: From weather to boundary-layer eddies, *J. Adv. Model. Earth Syst.*, *9*, 1572–1594, doi:10.1002/2017MS000960.

Received 4 MAR 2017
Accepted 19 APR 2017
Accepted article online 25 APR 2017
Published online 10 JUL 2017

Coupled mesoscale-LES modeling of a diurnal cycle during the CWEX-13 field campaign: From weather to boundary-layer eddies

Domingo Muñoz-Esparza[1], Julie K. Lundquist[2,3], Jeremy A. Sauer[1], Branko Kosović[1], and Rodman R. Linn[4]

[1]National Center for Atmospheric Research, Boulder, Colorado, USA, [2]Department of Atmospheric and Oceanic Sciences, University of Colorado Boulder, Boulder, Colorado, USA, [3]National Renewable Energy Laboratory, Golden, Colorado, USA, [4]Los Alamos National Laboratory, Los Alamos, New Mexico, USA

Abstract Multiscale modeling of a diurnal cycle of real-world conditions is presented for the first time, validated using data from the CWEX-13 field experiment. Dynamical downscaling from synoptic-scale down to resolved three-dimensional eddies in the atmospheric boundary layer (ABL) was performed, spanning 4 orders of magnitude in horizontal grid resolution: from 111 km down to 8.2 m (30 m) in stable (convective) conditions. Computationally efficient mesoscale-to-microscale transition was made possible by the generalized cell perturbation method with time-varying parameters derived from mesoscale forcing conditions, which substantially reduced the fetch to achieve fully developed turbulence. In addition, careful design of the simulations was made to inhibit the presence of under-resolved convection at convection-resolving mesoscale resolution and to ensure proper turbulence representation in stably-stratified conditions. Comparison to in situ wind-profiling lidar and near-surface sonic anemometer measurements demonstrated the ability to reproduce the ABL structure throughout the entire diurnal cycle with a high degree of fidelity. The multiscale simulations exhibit realistic atmospheric features such as convective rolls and global intermittency. Also, the diurnal evolution of turbulence was accurately simulated, with probability density functions of resolved turbulent velocity fluctuations nearly identical to the lidar measurements. Explicit representation of turbulence in the stably-stratified ABL was found to provide the right balance with larger scales, resulting in the development of intra-hour variability as observed by the wind lidar; this variability was not captured by the mesoscale model. Moreover, multiscale simulations improved mean ABL characteristics such as horizontal velocity, vertical wind shear, and turbulence.

1. Introduction

Accurate modeling of boundary-layer phenomena requires simultaneous representation of a broad range of scales ranging from synoptic and mesoscale two-dimensional eddies down to three-dimensional boundary-layer turbulence that develops in the near-surface region. In the past 5 years, efforts targeting dynamical downscaling of atmospheric numerical weather prediction (NWP) models beyond the mesoscale regime have started to emerge. These efforts pursue a variety of applications including improved wind field variability for wind energy forecasting [*Liu et al.*, 2011], hydrometeorological predictions [*Talbot et al.*, 2012], particulate dispersion [*Joe et al.*, 2014], orographic clouds and precipitation [*Chu et al.*, 2014], anthropogenic pollution particle dispersion [*Cécé et al.*, 2016], and daytime complex terrain flows [*Rai et al.*, 2016], among others. While these examples all utilized the Weather Research and Forecasting (WRF) model nesting capabilities (both for the mesoscale and microscale modeling), dynamical downscaling can be also performed using an off-line coupling to a large-eddy simulation (LES) model. In the latter, atmospheric fields are extracted from the mesoscale NWP model solution and are imposed as boundary conditions on the LES solver. The off-line approach has also been successfully applied to problems such as fine-scale urban dispersion [*Wyszogrodzki et al.*, 2012] and improved forecasts of sea-breeze horizontal convective rolls [*Chen et al.*, 2015].

While dynamical downscaling presents an attractive approach to improve modeling results through inclusion of explicitly resolved turbulence interactions, several modeling aspects require careful attention. One of them

is the onset of turbulence in an LES domain forced by a parent NWP mesoscale solution. As demonstrated by *Mirocha et al*. [2014] and *Muñoz-Esparza et al*. [2014a, 2015] among others, turbulence does not develop instantaneously in the LES domain when forced by a smooth mesoscale flow. Instead, turbulence requires extensive fetches to naturally emerge. This under-developed or transitional state not only affects energy spectra and turbulence-related magnitudes but also modifies the structure of the simulated atmospheric boundary layer (ABL). Recently, *Markowski and Bryan* [2016] have reported that LES without properly developed turbulence produces unrealistic near-surface vertical wind profiles containing excessive vertical wind shear (previously noticed by *Muñoz-Esparza et al*. [2014a], see their Figure 12). These idealized studies focused on homogeneous ABLs over flat terrain. However, recent works involving more complex forcings scenarios have confirmed the importance of developed turbulence at the inflow boundaries of an LES domain. In this regard, *Jähn et al*. [2016] showed that the lack of resolved inflow turbulence markedly affects cloud properties in the downwind area of Barbados island and generates wave-like structures in the upwind area that form artificial convergence lines. Similarly, *Sauer et al*. [2016] found that in the context of mountain-wave flows, a weaker critical layer that is less effective in constraining the upward propagation of trapped lee waves develops in the absence of properly spun-up ABL turbulence, as well as stronger shooting flows and weaker downhill rotors. Moreover, and even in the case of an urban environment where one may expect forcing from the buildings to provide reasonable results, *Lee et al.* [2016] have shown that the lack of developed inflow turbulence results in turbulence-void patches that affect lateral and top-down turbulent transport mechanisms, impacting important aspects of the velocity field such as recirculation zones and flow convergence in street canyons.

Beyond questions of appropriate "triggering" of turbulence in an inner domain, another critical aspect of multiscale simulations is the resolution at which to switch from the mesoscale one-dimensional planetary boundary layer (PBL) scheme (turbulence is fully parameterized) to a LES subgrid-scale (SGS) three-dimensional mixing scheme (most energetic eddies are resolved and eddies smaller than the grid size are parameterized). In particular, several studies have demonstrated that mesoscale 1D PBL schemes result in the appearance of "under-resolved" or "partly resolved" convective structures that are a numerical artifact arising from the violation of their underlying horizontal-homogeneity assumption [e.g., *Honnert et al*., 2011; *Zhou et al*., 2014; *Ching et al*., 2014]. While scale-aware [*Shin and Hong*, 2015; *Ito et al*., 2015] and three-dimensional PBL parameterizations [*Jiménez and Kosović*, 2016] should alleviate this effect, there is not yet a robust approach that has been shown to improve this aspect and that has been validated in a wide range of atmospheric conditions. Due to these constrains and motivated by the findings from the current study, *Mazzaro et al.* [2017] recently investigated the impact of these partly resolved structures when nested into an LES domain. The authors found that the presence of these structures delays the establishment of developed turbulence as the mesoscale parent resolution is coarsened and also affects the length scales of cellular convection. In addition, *Rai et al*. [2016] observed convective rolls emerging from a fine resolution mesoscale parent domain ($\Delta = 1.35$ km) that strongly affected the nature of the structures developed in the nested LES domain, which evolved into a more cellular-like structure depending on the distance to the inflow planes.

In this paper, we present the first coupled mesoscale-to-LES simulations of a diurnal cycle enabled by the cell perturbation method [*Muñoz-Esparza et al*., 2014a, 2015, see section 4 for more details] and validated using field data from the CWEX-13 field experiment [*Lundquist et al*., 2014]. The structure of the reminder of the paper is as follows. Section 2 describes the CWEX-13 campaign used in this study. The numerical model setup and mesoscale sensitivity to initial and boundary conditions and PBL scheme are presented in section 3. The coupling strategy is presented and demonstrated in section 4. The accuracy of the multiscale modeling results is evidenced through comparison to wind-profiling lidar and near-surface sonic anemometer measurements in section 5. Finally, the main findings are summarized in section 6.

2. Data Set: The CWEX-13 Field Campaign

The series of Crop-Wind Energy Experiments [*Rajewski et al*., 2013; *Rhodes and Lundquist*, 2013; *Rajewski et al*., 2014] explored the interaction of wind turbines with intensive agriculture. The CWEX-13 field campaign took place in summer 2013 [*Lundquist et al*., 2014; *Takle et al*., 2014] and featured wind-profiling lidars, a Leosphere 200S scanning lidar, and several surface flux stations to explore the interaction of wakes from

multiple wind turbines with intensive agriculture in a location subject to strong variations in atmospheric stability and the resulting flow phenomena such as nocturnal low-level jets [*Vanderwende et al*., 2015].

Here we focus on data from the wind-profiling lidar (WC1) and surface flux station located near the southwestern border of the wind farm, approximately half way between the northern end and southern end of the wind farm (see Figure 1). The turbines are laid out roughly as a parallelogram with major axis extending from the northwest to the southeast. Approximately 2.8 km to the southeast of the lidar at a heading of 146°, a row of turbines begins and extends further to the east. Approximately 3.8 km to the northwest at a heading of 275°, a row of turbines begins and extends further to the west. Therefore, in southeasterly (150°) to westerly (275°) flow conditions, the lidar samples flow unmodified by wind turbines. Land use within the wind farm is devoted to large fields of corn (height 1–2 m) and soybeans (height 0.3–0.8 m) except for four small villages, occasional riparian regions, and widely scattered farmsteads with few trees and buildings.

The WINDCUBE v1 profiling lidar samples line-of-sight (LOS) velocities sequentially in four cardinal directions along a beam approximately 28° from vertical. Along the beam, 10 range gates centered on 40, 60, 80, 100, 120, 140, 160, 180, 200, and 220 m above ground level (AGL) are simultaneously sampled. Hereafter, all the vertical distances are AGL unless specifically specified otherwise. The LOS velocities from the four beams are combined to estimate the three components of the flow. This approach assumes homogeneity for 4 s across the cone defined by the four beams; the resulting uncertainty can be quantified in complex terrain [*Bingöl et al*., 2009] and inhomogeneous flow [*Rhodes and Lundquist*, 2013; *Lundquist et al*., 2015].

From the extent of the CWEX-13 campaign (late June through early September, 2013), a period characterized by clear sky conditions with a strong diurnal variation, wind direction, ϕ, within the boundary layer in the range $180° < \phi < 250°$, and good data quality both for the wind lidar and surface measurements described here after, was chosen. While the CWEX-13 main purpose was to study wind farm effects, for the selected case here, the WC1 wind lidar and ISU surface flux station measured undisturbed flow conditions. Therefore, these measurements are used for multiscale modeling validation in the present study. Data quality checks of the lidar consisted of: availability >95%, carrier-to-noise ratio (CNR) > -22 dB. The selected period meeting the previous criteria was the 26 August. Figure 2 shows lidar measurements of wind speed and wind direction on the 26 August. The structure of the ABL during the selected period consists of an initial nighttime phase (0000–1200 UTC, or 1900–0700 Local Time) characterized by both a strong vertical wind shear and veer. As shown by the observations of *Vanderwende et al*. [2015] and the mesoscale

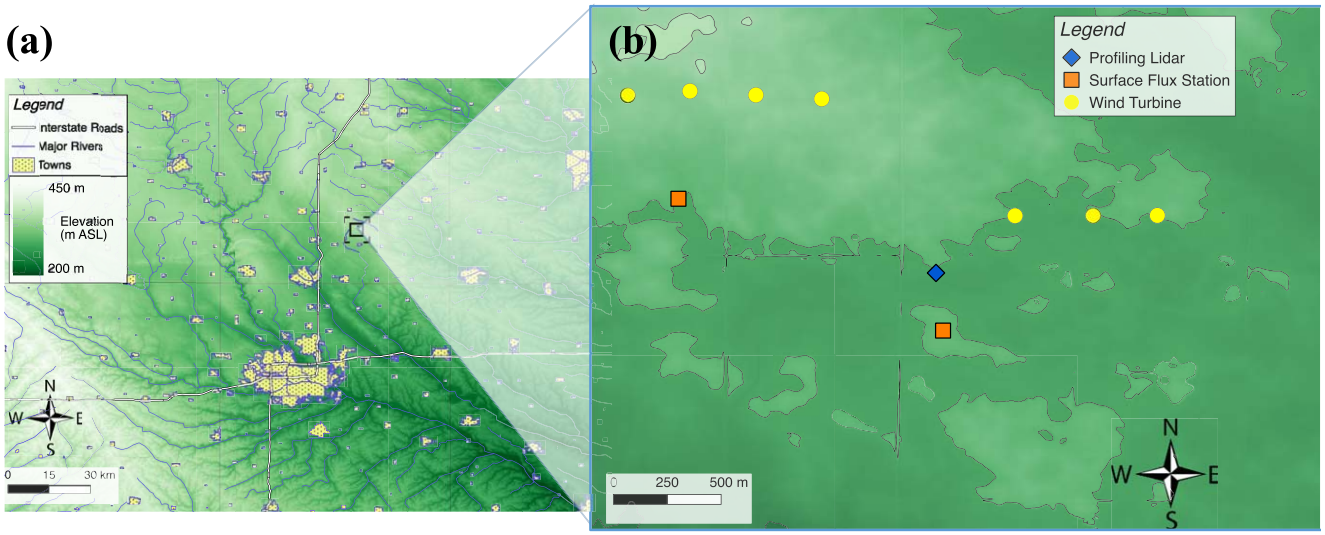

Figure 1. Topographic map of (a) north-central Iowa and (b) a 3 km × 3 km portion of the domain of the CWEX-13, with 10 m elevation contours. The highest elevation in the domain (northwest corner) is 360 m above mean sea level (MSL). The lowest elevations are between 330 and 340 m above MSL. Seven turbines, two surface flux stations, and one lidar (WC1) appear in this domain.

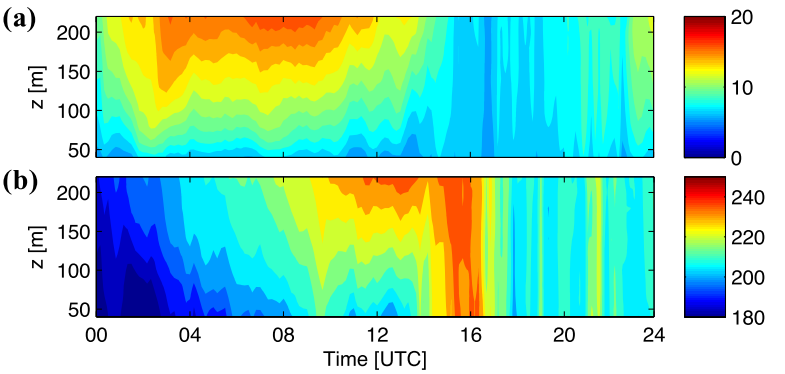

Figure 2. Time-height contours of (a) 10 min averaged wind speed (m s^{-1}) and (b) wind direction (°) measured by the WINDCUBE v1 profiling lidar (WC1) on 26 August 2013.

modeling of the next section, this strong shear is due to the presence of a low-level jet. After 1200 UTC (0700 LT), stability starts to turn convective and a well-mixed ABL occurs, together with a homogenization of the wind direction with height. During the last 4 h, 2000–2400 UTC (1500–1900 LT), an increase in wind speed likely due to large-scale forcing is present, and shear begins to develop at the last 2 h due to the ABL becoming stably-stratified again.

Surface flux stations also monitored the surface-driven stability variations. Located 355 m to the SSE (8°E of S) of WC1, ISU deployed a surface flux station (ISU3). A sonic anemometer (Campbell Scientific CSAT3) with infrared gas analyzer (EC150) was mounted at 8 m on a boom facing due south, collecting data at 20 Hz. Two three-cup anemometers (Campbell Scientific 03101-L) were also mounted at 5 and 10 m. A wind vane (R. M. Young 03301) was also located at 10 m. Temperature and relative humidity were both measured at 5 and 8 m with the HC2S3 (Rotronic) probe (facing north). Radiation was measured at the surface flux station north-west of WC1 with a Kipp and Zonen net radiometer, which provides both incoming and outgoing shortwave and longwave radiation measurements. After applying a sonic tilt correction algorithm [*Wilczak et al*., 2001], sonic data were averaged over 20 min intervals for flux estimates. These flux estimates can be used to calculate the Obukhov length, L, to quantify atmospheric stability through the simulation period.

Figure 3 shows inverse Obukhov length scaled with the sonic anemometer height, $zL^{-1} = -z\kappa g\langle w'\theta'\rangle / u_*^3\theta_s$, where κ is the von Karman constant (=0.41), g is the acceleration due to gravity (=9.81 $m^2\ s^{-2}$), $\langle w'\theta'\rangle$ is the turbulent heat flux, $u_* = [\langle u'w'\rangle^2 + \langle v'w'\rangle]^{1/4}$ is the friction velocity, and θ_s is the sonic temperature. The dimensionless parameter $z\ L^{-1}$ can express the competing roles of shear and buoyancy in the production and destruction of turbulence. As seen in Figure 3, buoyant suppression of turbulence dominates the first 12 h, with strongest stability around 0200 and 1100 UTC (2100 and 0600 LT). These events of stronger stratification are associated with periods where wind lidar observations reported a decrease of vertical wind speed shear (Figure 2), in turn reducing mechanical turbulence production and making nighttime buoyancy suppression dominant. Throughout the bulk of the night (0200–1100 UTC), measurements of $z\ L^{-1}$ indicate

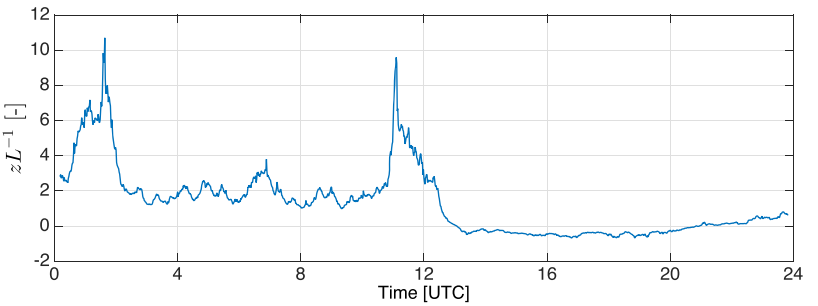

Figure 3. Time evolution of inverse Obukhov length on 26 August 2013 derived from turbulent fluxes obtained from the sonic anemometer, z = 8 m, located at the surface flux station ≈250 m south-east of the WC1 wind lidar.

slightly stable conditions given the presence of strong vertical shear. Soon after sunrise (≈0630 LT or 1230 UTC), the atmosphere becomes unstable through the rest of the day. The transition between nighttime and daytime conditions corresponds with $z\,L^{-1} \approx 1$ instead of ≈0 (further corroborated by the inflection in the time evolution of 8 m temperature shown in section 5). Such shifting is attributed to the use of sonic temperature for the calculation of L, which accounts only partially for the humidity flux contribution to atmospheric stability [*Barthelmie et al*., 2010].

3. WRF Setup and Mesoscale Modeling Sensitivity Analysis

Mesoscale and multiscale simulations of the selected diurnal cycle from the CWEX-13 field experiment were performed using the Advanced Research WRF model version 3.6, a nonhydrostatic, fully compressible with acoustic wave modes filtering, Euler equations solver that includes nesting and three-dimensional mixing capabilities [*Skamarock and Klemp*, 2008; *Skamarock et al*., 2008]. In order to concurrently represent scales from the synoptic range down to ABL turbulent eddies, a five-domain one-way nested setup was designed. The first three domains, D01–D03, with horizontal resolutions of Δ=8.91, 2.97, 0.99 km, utilized a PBL scheme for turbulence closure (Figure 4a). The number of grid points in the zonal and meridional directions for each of the mesoscale domains was: $400 \times 410, 460 \times 400$, and 571×511, respectively. A two-dimensional Smagorinsky closure was applied in the mesoscale domains [*Smagorinsky*, 1963], where the eddy viscosity depends on horizontal deformations, grid size, ℓ, and the so-called Smagorinsky constant, c_s: $K_h = c_s^2 \ell^2 [0.25(D_{11} - D_{22})^2 + D_{12}^2]^{1/2}$. Two additional nested domains shown in Figure 4b, D04 and D05, with resolutions of $\Delta = 90$ and 30 m, respectively, were used for convective conditions (1200–0000 UTC), while proper representation of stably-stratified ABL turbulence required finer resolution across the innermost domain, D05, with Δ=8.2 m, as revealed from the analysis presented in section 4.2 (0000–1200 UTC). Domains D04 and D05 utilized a three-dimensional LES turbulence closure including a prognostic TKE equation [*Lilly*, 1966, 1967] and consisted of 826×826 grid points in the horizontal directions.

A grid refinement ratio of 11 was used between domains D03 and D04, where the transition from the PBL scheme to three-dimensional LES occurs. While this grid refinement ratio is larger than the commonly utilized factor of 3, this value was specifically selected to avoid unrealistic modeling at resolutions within the terra incognita regime [*Wyngaard*, 2004] where neither PBL schemes nor LES closures are appropriate. For

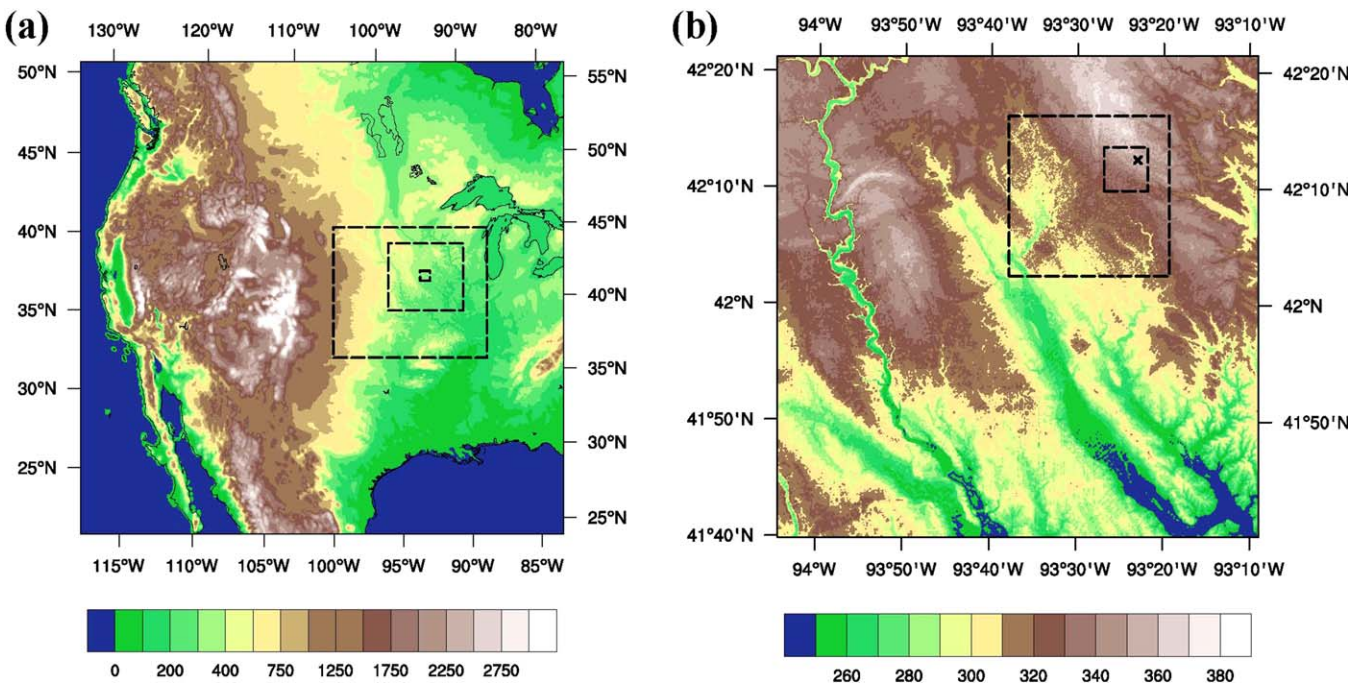

Figure 4. WRF domains with terrain elevation above mean sea level (m). (a) Mesoscale domains D01, D02, and D03, with Δ=8.91, 2.97, 0.99 km, respectively, boundaries of domain D04 are indicated for reference. (b) LES domains, D04 and D05, $\Delta = 90$, 30/8.2 m. The cross denotes the location of the WC1 wind-profiling lidar.

all the domains, the vertical coordinate was discretized using 73 grid points, with fine vertical resolutions within the lowest 2 km, $\Delta z \approx 10$–142 m (42 vertical levels), in order to have a grid size allowing explicit resolution of three-dimensional turbulence features. Moreover, fine vertical grid spacing has been shown to be required for PBL schemes to avoid overestimating observed low-level jet heights and over diffusing the jet structure [*Muñoz-Esparza*, 2013]. For $z > 2$ km, grid spacing was progressively increased to span the remaining vertical domain extent with the model top placed at $p_t = 100$ hPa ($z \approx 14$ km).

As seen from Figure 4, LES domains were shifted southwest from the experimental site to ensure a sufficient fetch for turbulence generated by the cell perturbation method to equilibrate before reaching the location of the lidar and surface flux station. Also, higher resolution terrain topography data sets from the shuttle radar topography mission (SRTM) [*Farr et al*., 2007] were used for domains D04 and D05, with resolutions of 3 arc sec (≈90 m) and 1 arc sec (≈30 m), respectively. Soil and land use data were specified at a resolution of 30 arc sec (≈1 km). While the different resolution of soil/land use and terrain could impose a slight bias in the results, the higher resolution terrain data is desirable to have an appropriate turbulence forcing from the topography at the grid scale. Domains D01–D03 were initialized at 0000 UTC on 25 August for the mesoscale structures to have time to develop and equilibrate from the initial synoptic forcing. In order to allow for proper ABL spin-up preceding the period of interest, the LES domains were initialized at 1800 UTC on 25 August.

Physical parameterizations include the longwave rapid radiative transfer model (RRTM) [*Mlawer et al*., 1997], shortwave Dudhia scheme [*Dudhia*, 1989], Kain-Fritsch cumulus parameterization [*Kain*, 2004] (only used by the Δ=8.91 km domain), and the WRF single-moment three-class microphysics scheme [*Hong et al*., 2004]. The unified Noah land-surface model [*Chen and Dudhia*, 2001] was used in all the simulations, while the surface layer parameterization option was set according to the selected PBL scheme, with all of them based on the Monin-Obukhov similarity theory [*Monin and Obukhov*, 1954]. For the LES domains, the revised surface-layer scheme from *Jiménez et al*. [2012] was used.

Sensitivity experiments were performed by varying the reanalysis used for initial and boundary conditions (IBCs) using three different data sets: the North American Regional Reanalysis (NARR: 3 h, $\Delta = 32$ km, 30 vertical levels) [*Mesinger et al*., 2006], the Interim European Centre for Medium-Range Weather Forecasts Re-Analysis (ERA-Interim: 6 h, $\Delta \approx 0.7°$, 38 vertical levels) [*Dee et al*., 2011], and Global Forecast System FNL observational analysis (FNL: 6 h, $\Delta \approx 1.0°$, 27 vertical levels) [*NCEP*, 2017]. For each of the IBC data sets five PBL schemes were exercised: Yonsei University (YSU) [*Hong et al*., 2006], Mellor-Yamada-Janić (MYJ) [*Janjić*, 1994], Mellor-Yamada-Nakanishi-Niino (MYNN) [*Nakanishi and Niino*, 2006], Quasi Normal Scale Elimination (QNSE) [*Sukoriansky et al*., 2005], and QNSE combined with a nonlocal eddy-diffusivity mass-flux (EDMF) scheme for convective conditions. In total, 15 experiments were conducted to identify the most accurate mesoscale forcing conditions to be applied at the LES domains (sensitivity tests included the three mesoscale domains, D01–D03). From this analysis it was found that in general, the IBCs from the NARR data set increased the root-mean-square error of wind speed by ≈1.0 m s^{-1} and wind direction by ≈7.0° (average over the lidar measurement heights) with respect to the other two reanalysis data sets. ERA-Interim and FNL resulted in a similar performance, with the latter having reduced errors by 25%. Among PBL schemes, YSU exhibited the largest errors, increased by a factor of 2 relative to the other schemes. In particular, YSU tended to overestimate (underestimate) horizontal wind speed magnitude during stable (convective) conditions. Also, the QNSE-EDMF scheme consistently increased the error in wind speed by 20% compared to the standard QNSE irrespective of the IBCs. Combination of FNL IBCs with the MYNN PBL scheme resulted in the lowest errors (1.2 m s^{-1}, ≈7.5°), and so this combination was selected for the multiscale simulations shown in the remainder of the manuscript.

Multiscale simulations performed herein were computationally intense. Computing time required to simulate 1 h of physical time was approximately 40,000/60,000 CPU hours (for D05 resolutions of 30 and 8.2 m, respectively), on a cluster composed of dual 8 core Intel Xeon (Sandy Bridge) processors with InfiniBand. Therefore, the total computing time to run an entire diurnal cycle was 1.5×10^6 CPU hours.

4. Inflow Turbulence Generation Method and Coupling Strategy

As pointed out in the introduction, recent literature has highlighted the problems associated with LES models when inadequately resolved turbulence is provided to a microscale domain. In these cases, the

unbalanced resolved/SGS turbulent kinetic energy (TKE) partitioning leads to a degradation of simulated fields in spite of the expected benefit from the increased grid resolution. To solve such problem, we use the generalized cell perturbation method, which employs a novel stochastic approach based upon finite amplitude perturbations of the potential temperature field applied within a region near the inflow boundaries of the LES domain. The method was originally proposed by *Muñoz-Esparza et al*. [2014a] and uses appropriate thermal perturbations that trigger the formation of microscale three-dimensional motions characteristic of boundary-layer turbulence that are not present in the mesoscale regime. These three-dimensional flow features are initiated by breaking the two-dimensionality of the forcing mesoscale flow by adding vertical accelerations induced by potential temperature perturbations. The method results in an accelerated transition to a fully developed turbulent state and is computationally inexpensive.

On a follow-up manuscript, *Muñoz-Esparza et al*. [2015] identified the nondimensional parameters that minimize the transitional fetch required to reach the quasi-equilibrium solution (the generalized cell perturbation method). These parameters are namely the perturbation Eckert number, $Ec=U_g^2/(c_p\tilde{\theta}_{pm})$, and a perturbation time scale, $\Gamma=t_pU_1/d_c$. In the previous expressions, U_g is the geostrophic wind, c_p is the specific heat capacity at constant pressure, $\tilde{\theta}_{pm}$ is the maximum amplitude of the pseudo-random perturbations uniformly distributed in the range $[-\tilde{\theta}_{pm},+\tilde{\theta}_{pm}]$, t_p is the perturbation time at which the thermal perturbations are instantaneously applied, U_1 is the velocity magnitude from the NWP at the first vertical grid point that is imposed at the boundary of the LES domain, and d_c is the diagonal of the cell in the horizontal plane. An optimum $Ec = 0.2$ was found to result in the fastest generation of forcing-consistent turbulence through development of hairpin-like vortices that rapidly transition to developed streaks. The optimum perturbation time is derived from $\Gamma = 1$, ensuring the flow can be advected out of a perturbation cell before applying the next perturbation. Cells need to be large enough so the spatial scale belongs to the fully resolved inertial range of three-dimensional turbulence. Otherwise the excited scales cannot interact with the flow and rather are rapidly mitigated by the dissipative component of the advection scheme. For the WRF model, where the odd-order upwinding schemes have an effective resolution of $\approx 7\Delta x$ [*Skamarock*, 2004], we use square horizontal cells of $8\Delta x \times 8\Delta x$ grid points. Also, three horizontal rows of cells are used, as found to be the optimum configuration by *Muñoz-Esparza et al*. [2015].

The initial phases of conception and optimization of the cell perturbation method used canonical boundary layer scenarios for which reference quasi-equilibrium solutions can be obtained via simulation applying cyclic or periodic lateral boundary conditions. While these cases provide an optimal framework for the development of the method, the robustness of the inflow generation technique must be shown for more complex cases. Recent efforts have progressed the application and validation of the cell perturbation method to less idealized scenarios where field measurements were used to derive forcing conditions for the LES modeling [*Jähn et al*., 2016; *Lee et al*., 2016]. In these studies, LES with inflow turbulence triggered by the cell perturbation method showed good performance in reproducing the observed structure of the ABL and island-induced clouds, as well as velocity patterns in an urban area, respectively. Herein, we take another step forward and apply the cell perturbation method to a real diurnal cycle in fully coupled mode, i.e., atmospheric fields varying in both space and time are used as lateral boundary forcing on the LES domain and all the NWP model physics incorporated.

As recommended by *Muñoz-Esparza et al*. [2014a], perturbations are applied for $z_{CP} < 2/3z_i$, where z_i is the boundary-layer height. This is done to avoid interference with the stably-stratified capping inversion by the thermal perturbations, which could potentially trigger numerical instabilities. Therefore, z_{CP} must accommodate the diurnal evolution of z_i. Boundary-layer height is diagnosed in PBL schemes and used as part of the parameterization in ways that are scheme dependent. In the particular case of the MYNN scheme, z_i is derived using the following formulae: $z_i=z_{i,q}(1-wt)+z_{i,\theta}wt$, where $z_{i,\theta}$ is the height at which the virtual potential temperature is greater than the minimum at a given location by 1.5 K, $z_{i,q}$ is the height at which SGS TKE energy falls below 0.05 its maximum value, and wt is a blending function that depends on $z_{i,\theta}$ and a typical z_i for stable boundary layers. In order to a have an estimate of z_i from the mesoscale results that is less sensitive to the parameterization used by the PBL scheme, another criterion was considered. This criterion assigns z_i to the height of maximum $\partial\theta/\partial z$ during convective conditions and to the height of local maximum horizontal wind during stable conditions.

Figure 5 shows the results of all the different criteria used to estimate z_i. For these calculations, z_i estimates were averaged across the south and west LES inflow planes. From the morning transition until the time

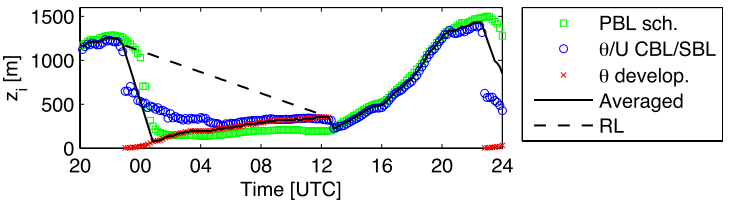

Figure 5. Comparison of boundary-layer height, z_i, estimated using different approaches for the period from 2200 UTC (1700 LT) on 25 August through 0000 UTC 27 August (1900 LT 26 August). The solid line indicates the value of z_i used to derive the required cell perturbation parameters. z_{RL} is the parameterized evolution of the residual layer height, with the perturbations in this layer decreasing exponentially from the onset (≈2300 UTC (1800 LT) 25 August) to 1% of the initial value by the end of the stably-stratified period (≈1300 UTC (0800 LT) 26 August).

where the maximum convection happens (largest z_i), the two criteria produce similar results. At later times, the correction of the PBL scheme z_i allows for a steeper decrease as convection starts to weaken. To reduce the uncertainty on the estimation of z_i, an average of the two criteria was used when the ABL was convective. However, we found that neither the PBL scheme nor the other criterion captured the growth of z_i from the ground resulting from the cooling at the surface during stable conditions. For that regime, $\partial\theta/\partial z$ is a best indicator of such phenomenology. We empirically determined a threshold of $\partial\theta/\partial z$=0.014 K m^{-1} to be a reasonable value for the particular case analyzed herein, which resulted in a z_i smoothly increasing toward the ABL height estimated by the two other criteria at the onset of morning convective instability (≈1300 UTC, 0800 LT). Therefore, such threshold was used to estimate z_i when the ABL was stably stratified (θ-development criterion). The horizontal wind speed at $z = z_i$ was used as an estimate for U_g to derive time-varying $\tilde{\theta}_{pm}$ corresponding to the optimum perturbation Eckert number, $Ec = 0.2$.

The proposed methodology will only generate turbulence within the ABL. However, turbulence in the residual layer is important for the development of the stable boundary layer [*Blay-Carreras et al.*, 2014]. In an attempt to represent the influence of residual layer turbulence on the growth and development of the stable ABL, we applied a second layer of perturbations during stable conditions in the range $[z_{CP}, z_{RL}]$. The upper limit of the residual layer, z_{RL}, was estimated as linearly varying in time within the interval delimited by zero heat flux crossing. In lieu of a better parameterization, the strength of the perturbations in the residual layer was decreased exponentially as occurs for the rate of energy decay of isotropic turbulence in the absence of external forcing [e.g., *Pope*, 2001], to 1% of the initial value by the end of the stably-stratified period (≈1300 UTC, 0800 LT). A better approach could be developed through a more systematic sensitivity analysis, however, such analysis is beyond the scope of the current study. Finally, it is worth mentioning that the first three vertical levels were not perturbed in order to avoid contamination of land-surface and surface-layer processes by the imposed thermal perturbations, which have the sole purpose of accelerating turbulence development and could otherwise negatively affect the energy budget at the surface.

4.1. Under-Resolved Convection and Turbulence Development in the LES Domains

In order to ensure the presence of a fully developed turbulent state for the period of interest: 0000 UTC 26 to 0000 UTC 27 August (1900 LT 25 to 1900 LT 26 August), multiscale simulations were initialized 6 h in advance (1800 UTC 25, 13 LT 25), so that this time period constitutes the spin-up phase for the LES domains (mesoscale spin-up is 24 h, as mentioned in section 3). In practice, it was observed that after 2–3 h turbulence had propagated across the entire domain for the case analyzed herein, but longer times may be required when the wind speeds are lower and/or the LES domain is larger. As seen from the time evolution of z_i plotted in Figure 5, the local maximum boundary-layer height during the period of interest is achieved around 2200 UTC, with a value of $z_{i,max} \approx 1500$ m. Figure 6 shows meridional velocity on a horizontal plane at $z = 100$ m corresponding to the first LES domain (D04, $\Delta = 90$ m) at 2200 UTC, and in which the cell perturbation method was not applied. This contour plot exhibits large coherent rolls driven by the finest resolution mesoscale domain (D03, $\Delta = 990$ m) persisting throughout most of domain D04 (75 km × 75 km). These rolls require large fetches to progressively begin to be distorted as resolved turbulence emerges. At that particular time, the ratio of boundary-layer height to Obukhov length, $-z_i L^{-1} \approx 12$, is within the range of values for which convective rolls have been observed in the atmosphere [e.g., *LeMone*, 1973; *Grossman*, 1982; *Weckwerth et al.*, 1999]. *Honnert and Masson* [2014] demonstrated by filtering LES results of convective boundary layers (CBLs) that in the case of a sheared CBL, horizontal mesoscale resolutions need to be larger than ≈3z_i to avoid one-dimensional PBL schemes to introduce unphysical structures in the flow field (i.e.,

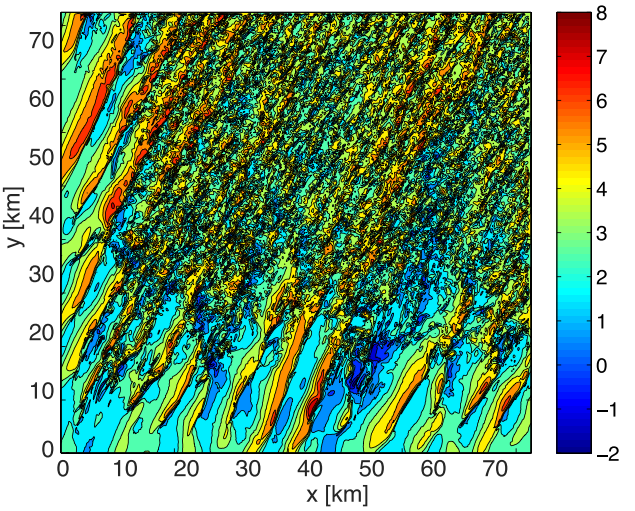

Figure 6. Zonal velocity (m s^{-1}) on a horizontal plane at $z = 100$ m on the first LES domain (D04, $\Delta = 90$ m) at 2200 UTC (1700 LT) 26 August. Cell perturbation method not applied.

horizontal-homogeneity assumption is violated). For the results displayed in Figure 6 the associated limit on resolution would be $\Delta = 3600$ m, which is 4 times larger than domain D03 horizontal resolution. In the zonal and vertical velocity components at the southern boundary of domain D04 (Figures 7a and 7b), the artificial nature of the rolls is manifested as a coherent pattern characteristic of inadequate resolution of three-dimensional structures [*Zhou et al.*, 2014; *Ching et al.*, 2014].

As mentioned in section 3, mesoscale models apply a two-dimensional Smagorinsky closure in order to represent subgrid-scale turbulent diffusion [*Smagorinsky*, 1963]. The use of a nonlinear eddy viscosity approach was originally proposed by *Von Neumann and Richtmyer* [1950] as a dissipative mechanism to stabilize the solution in the computation of shock waves and was later adopted by Smagorinsky as a two-dimensional turbulent closure for a NWP model [*Smagorinsky*, 1990]. The so-called Smagorinsky constant, c_s, has a value that allows for the energy cascade in the mesoscale quasi-two-dimensional regime to be maintained, and it is typically set to 0.25 in WRF (≈0.2 is commonly used for two-dimensional and three-dimensional turbulence closures). However, these spurious under-resolved structures, which are three dimensional, cannot be properly balanced when a two-dimensional Smagorinsky turbulence closure is used, since turbulent diffusion is underestimated owing to the lack of contribution from the unconsidered vertical gradients. Therefore, and following the rationale that originated the nonlinear eddy viscosity approach [*Von Neumann and Richtmyer*, 1950], we increased c_s on domain D03 to prevent the instability induced by the upward heat flux at the surface to generate spurious three-dimensional motions in the mesoscale domain.

The effect of increasing c_s from the default 0.25 to 1.0 and 2.0 is shown in Figure 8, where the vertical velocity for different c_s values at $z = 500$ m is presented (approximately coincident with the half the vertical scale of the structures). By increasing c_s the amount of dissipation is larger and therefore the signature of the three-dimensional vertical updrafts and downdrafts is progressively damped, as anticipated. We found that $c_s = 2.0$ removed any significant contribution of under-resolved convection from the mesoscale domain (see

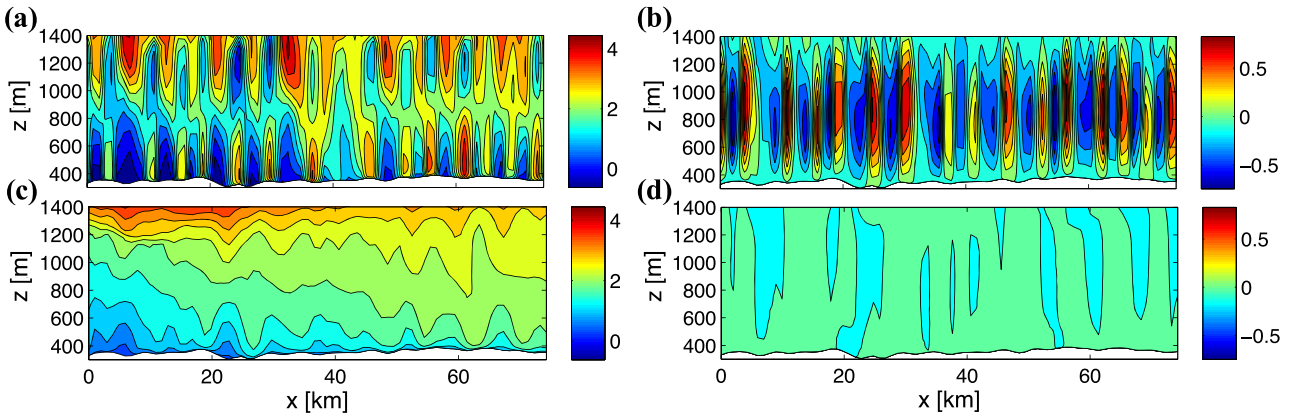

Figure 7. (a, c) Zonal and (b, d) vertical velocity components (m s^{-1}) on the finest resolution mesoscale domain (D03) coincident with the southern boundary of the first LES domain for the default $c_s = 0.25$ (Figures 7a and 7b) and enhanced diffusion $c_s = 2.0$ (Figures 7c and 7d). Vertical coordinate in meters above mean sea level. The terrain is indicated by a white contour, with the terrain-atmosphere interface marked by solid black line.

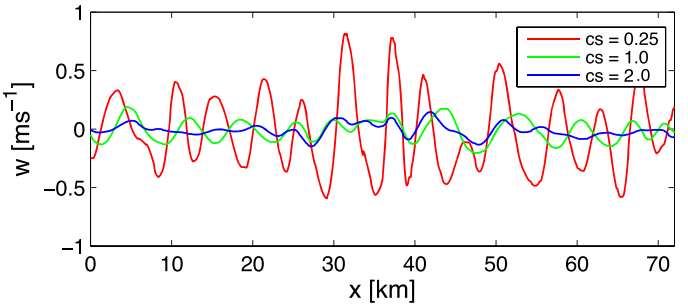

Figure 8. Vertical velocity along a line at $z = 500$ m on the finest resolution mesoscale domain (D03) coincident with the southern boundary of the first LES domain for $c_s = 0.25$, 1.0, and 2.0, at 2200 UTC 26 August (1700 LT).

Figures 7c and 7d). The maximum vertical velocity magnitude is decreased from the original value of $|w| = 0.5$ m s^{-1} down to less than one tenth of that value, $|w| < 0.05$ m s^{-1}, while not affecting the mean ABL structure. Any further increase of c_s had the negative impact of making the ABL velocity profiles more neutral (not shown). We speculate that this effect is most likely due to an enhanced horizontal mixing that starts to dominate over the vertical counterpart, which is no longer enough to create a well-mixed ABL. For the particular case analyzed herein, $c_s = 2.0$ is an appropriate choice, however such value may be case dependent and needs to be investigated in more detail if a more general value of c_s should be defined for grid resolutions within the terra incognita [*Wyngaard*, 2004], since it is expected to depend on grid resolution and the strength of convection.

Cell perturbation is required to trigger generation of turbulence without large upwind fetches. Figure 9 shows zonal velocity (a, b) and potential temperature (c, d) on horizontal planes at $z = 100$ and 500 m, respectively, at 2200 UTC (1700 LT) 26 August. In Figure 9d, the spatial structure of the imposed potential

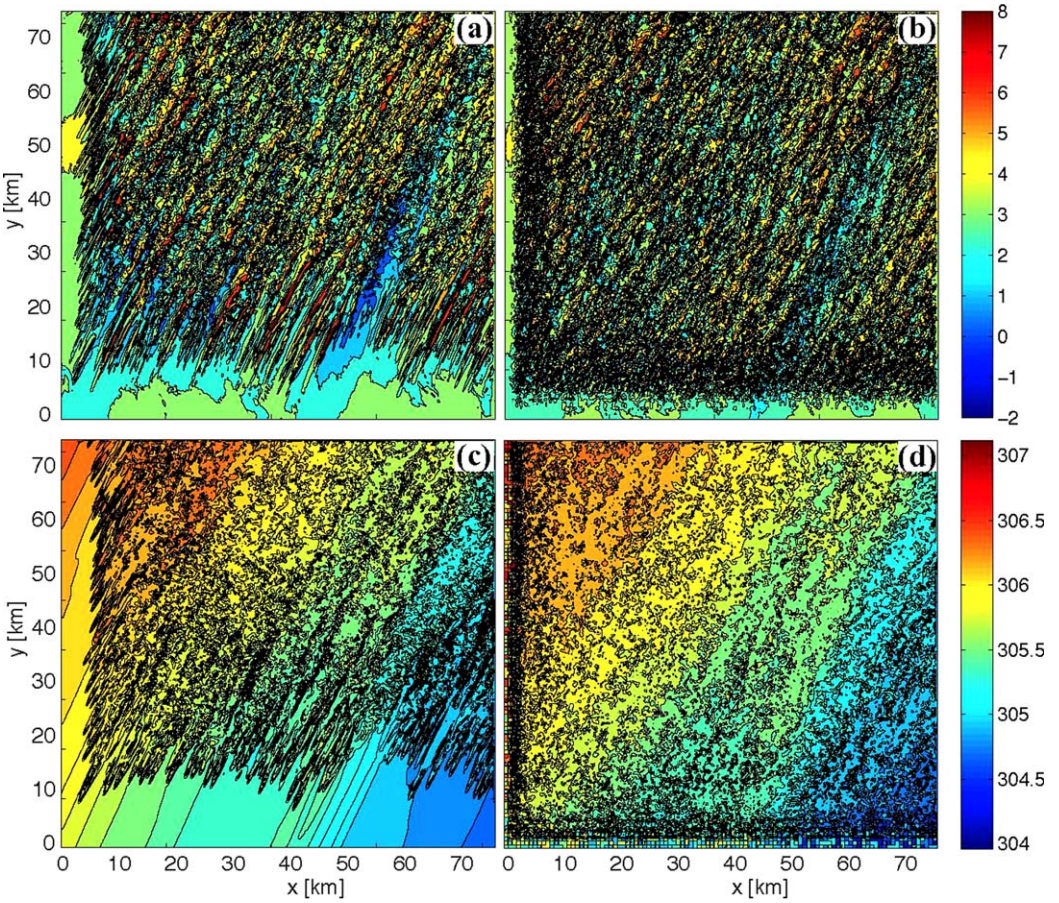

Figure 9. Zonal velocity (m s^{-1}) on a horizontal plane at $z = 100$ m corresponding to the first LES domain (D04, $\Delta = 90$ m) at 2200 UTC (1700 LT) 26 August (a) without and (b) with the cell perturbation method. Same for potential temperature (K) on (c, d) a horizontal plane at $z = 500$ m.

temperature perturbations consisting of three rows of bidimensional cells with 8 × 8 grid points size along the southern and western boundaries of the LES domain D04 is clearly observed. Even in the peak of convection strength yielding a maximum z_i, the case without applying the cell perturbation method results in larger fetches to start generating turbulence. The unperturbed case results in a much larger delay in the onset of turbulence with increasing height, with the temperature at $z = 500$ m lagging behind by ≈10 km. The case that uses the cell perturbation method results in a rapid and homogeneous turbulence development across the entire domain while the unperturbed case has an irregular development pattern and displays coherent transitional structures over large distances into the domain ($10 < y < 35$ km). Moreover, the cell perturbation case exhibits streamwise-aligned convective rolls of alternating high- and low-speed regions associated with updrafts and downdrafts secondary circulations in the spanwise direction, respectively. Also, both velocity and potential temperature contours demonstrate that there are regions where the flow leaves the LES domain still presenting fingerprints of such transition (north-west corner of the domain).

To quantify the development of turbulence, y direction evolution of the energy spectra of zonal velocity is presented in Figure 10 for domain D04. At first, the unperturbed solution exhibits dramatic energy deficits when compared to the cell perturbation case, for $y < 10$ km from the southern inflow boundary (Figure 10a). Later, initially developing convective rolls are more coherent due to the lack of upstream resolved turbulent fluctuations, yielding to an energy overshoot at large scales seen at $y = 25.0$ km (Figure 10b), which takes a distance of $y \approx 45.0$ km to finally equilibrate. The energy spectra demonstrates the coexistence of a mesoscale energy spectrum with a $-5/3$ slope followed by a production region (slope -1, $1 \times 10^{-3} < k < 8 \times 10^{-3}$ m^{-1}) and a final three-dimensional inertial range with $-5/3$ slope again. In contrast, mesoscale domain D03 displays a larger portion of $-5/3$ slope with no presence of three-dimensional turbulence production (slope -1). While perfect matching of theoretical mesoscale and turbulent energy spectra cannot be exactly determined due to the expected variability in the energy spectra at an instantaneous time in a particular location, energy distribution clearly exhibits the transition between the different regimes. It is worth bringing to attention that in the presence of under-resolved convection (Figure 6, cell perturbation not applied), the onset of turbulence is further delayed. In spite of the presence of velocity and temperature gradients that one could expect to help produce turbulence, these coherent mesoscale structures are in fact too energetic and therefore are inappropriately maintained for longer fetches before proceeding to break apart. This finding has motivated the recent work by *Mazzaro et al.* [2017], to quantify the impact of these under-resolved structures on a nested LES domain.

Finally, Figure 11 displays wind speed and energy spectra along a horizontal plane at $z = 50$ m corresponding to the second LES domain, D05, with a grid refinement ratio of 3 ($\Delta = 30$ m). There is a development region near the southern inflow boundary, as has been observed in idealized studies of LES nested within

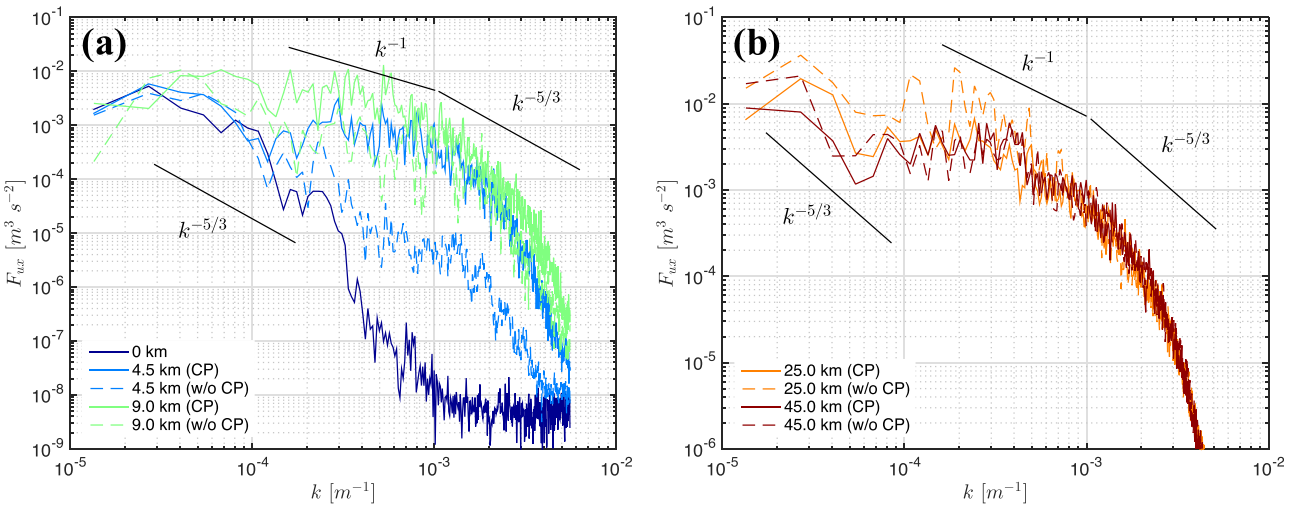

Figure 10. Energy spectra of zonal velocity along the x direction at several locations from $y = [0, 4.5, 9.0, 25.0, 45.0]$ km at $z = 100$ m corresponding to the first LES domain (D04, $\Delta = 90$ m) at 2200 UTC (1700 LT) 26 August. Spectra are calculated along the x direction and averaged over (a) 10 or (b) 50 grid points in the y direction. Results with (solid lines) and without (dashed lines) applying the cell perturbation method.

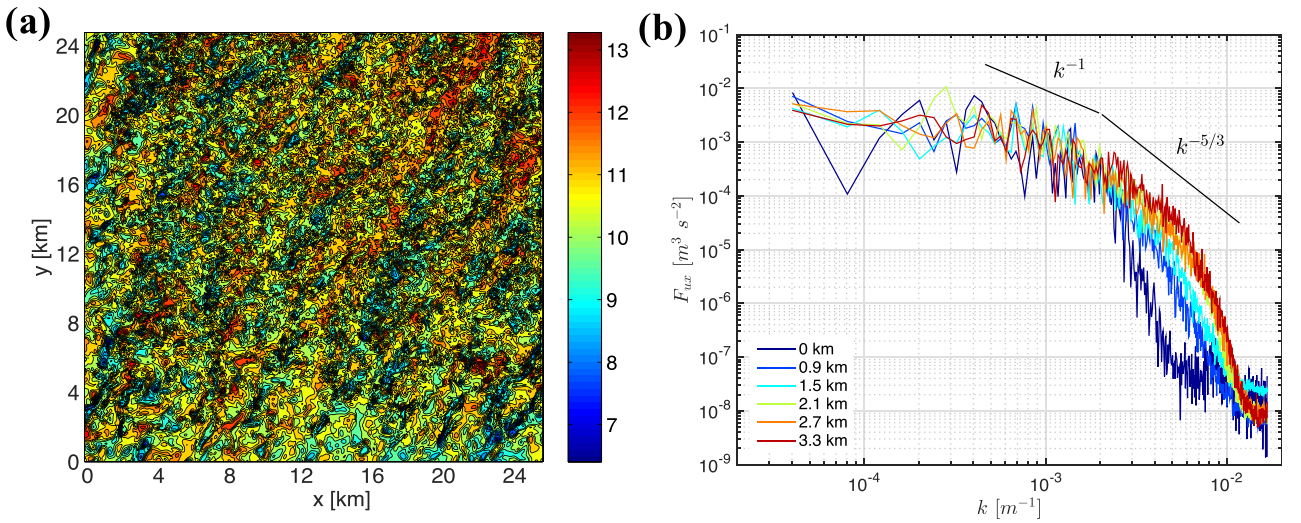

Figure 11. (a) Wind speed (m s^{-1}) on a horizontal plane at $z = 500$ m corresponding to the second LES domain (D05, $\Delta = 30$ m) at 2200 UTC (1700 LT) 26 August. (b) Energy spectra along the x direction at several locations $y = [0, 0.9, 1.5, 2.1, 2.7, 3.3]$ km (blue to red on a jet color scale), averaged over 25 grid points in the y direction.

LES [*Mirocha et al*., 2013; *Muñoz-Esparza et al*., 2014b]. Such a region requires a shorter fetch to reach a quasi-equilibrium state compared to the mesoscale-to-LES transition (D03–D04), however, in both cases it corresponds to about 100 grid points. A nested SGS TKE boundary condition is used for the second LES, as it was shown by *Muñoz-Esparza et al*. [2014b] to improve from the zero SGS TKE used by default in WRF. The flow in domain D05 equilibrates after approximately 2.7 km, maintains the already developed production range established by domain D04, and extends the $-5/3$ inertial range up to a wavelength of 6–8Δ associated with the implicit filtering of the upwinding discretization scheme of the advection operator. For larger refinement ratios for the second LES domain (up to 11), the transition gets progressively delayed to a further distance from the inflow boundary. We attribute this effect to the increase in the gap between the smallest turbulent scale resolved by the first LES and the range of scales that become resolvable by the second LES domain (not shown), which becomes somewhat like a mesoscale-to-LES transition for large refinement ratios. Therefore, we recommend the use of a ratio of three to minimize the transition fetch, since there is no method to date that deals with LES-to-LES transition including grid refinement.

4.2. Grid Resolution Requirements in Stably Stratified Conditions

A first attempt to resolve turbulence during the stably-stratified portion of the simulated diurnal cycle (0000–1200 UTC, 1900–0700 LT) was made using the setup previously described. However, after 0100 UTC (2000 LT) neither the first LES domain ($\Delta = 90$ m) nor the second LES domain ($\Delta = 30$ m) were able to develop and maintain an inertial range energy cascade. Instead, thermal instabilities created by the cell perturbation method were rapidly dissipated after the perturbations were advected out of the perturbation region, even when the cell perturbation method was applied at domain D05. To overcome this issue, the grid size of domain D05 was reduced by a factor of 11 from D04, $\Delta = 8.2$ m (smaller domain in Figure 4a). Horizontal contours of wind speed and vertical velocity at $z = 70$ m corresponding to domain D05 with the increased resolution are displayed in Figure 12, valid at 0800 UTC (0300 LT) 26 August. These velocity contours show the sequence by which the transition to turbulence happens. At first, potential temperature perturbations are applied in the perturbation region. Within the majority of this region, the velocity field remains barely unaffected. Then, temperature gradients induce vertical accelerations that immediately transfer energy to the horizontal components thus creating three-dimensional structures (see the reduced turbulence-void area on the vertical velocity contour). In this case, the signature of the perturbations appears to persist longer than in convective conditions, perhaps due to the presence of a low-level jet that induces a larger than geostrophic wind speed that in turn amplifies the strength of the imposed perturbations. Nevertheless, the flow progressively equilibrates and the influence of the perturbations vanishes entirely. The vertical velocity field exhibits regions where variability is low, but even for the largest distance

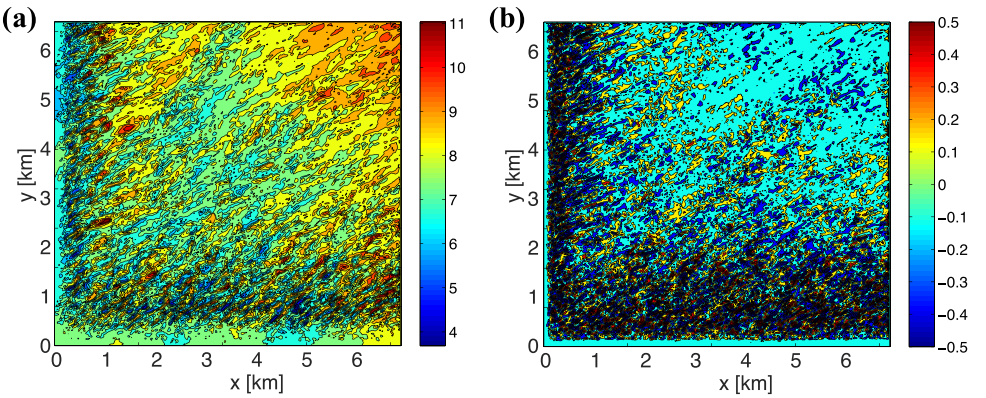

Figure 12. (a) Wind speed and (b) vertical velocity (m s^{-1}) on a horizontal plane at $z = 70$ m corresponding to LES domain D05 with increased resolution (Δ=8.2 m). Snapshot valid at 0800 UCT (0300 LT) 26 August. Cell perturbation method applied.

from the inflow in this south-westerly flow, there is never a permanent cessation of turbulence, which confirms the appropriateness of the grid resolution. These patches, characterized by a less turbulent activity, correspond to global intermittency phenomenon that occurs in stably-stratified ABLs [*Mahrt*, 1989].

The spectra for these simulations further demonstrate that finer resolution is required for stable simulations. Energy spectra of vertical velocity at $z = 75$ m at 0800 UTC (0300 LT) 26 August is shown in Figure 13. When horizontal grid resolution is $\Delta = 30$ m (Figure 13a), the imposed potential temperature perturbations do not result in a sustained production and energy cascade process. Instead, there is a progressive decay in energy content at isotropic small scales that nearly reverts to the energy content at the inflow boundary after $y = 24$ km. With an increased resolution of $\Delta = 8.2$ m (Figure 13b), domain D05 reaches an equilibrium state after the influence of the cell perturbation method disappears (half of the extent of the domain, $y \approx 3$ km), with an energy production, -1 slope, is followed by a reduced portion of inertial range scales with a $-5/3$ slope before numerical dissipation starts to decrease the energy content for $k \gtrsim 0.017$ m^{-1}. While Figure 13 reveals a developed spectrum of turbulent eddy sizes, the contours shown in Figure 12 indicate spatial variability in the level of patchiness observed in the velocity fluctuations, likely resulting from spatiotemporal heterogeneities in the forcing and the presence of global intermittency, the latter being further discussed in section 5.

In order to keep the computational cost of the multiscale simulations affordable, the total number of grid points constituting domain D05 was maintained. This means that the horizontal extent of the domain was

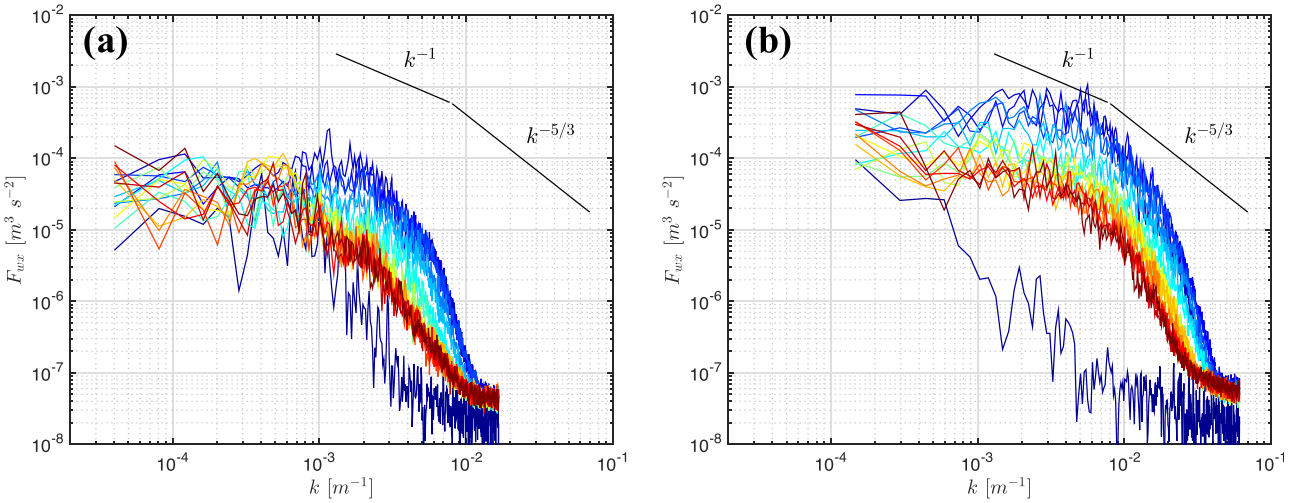

Figure 13. Energy spectra of the vertical velocity component along the *x* direction at $z = 75$ m at 0800 UCT (0300 LT) 26 August. Spectra are calculated along the *x* direction and averaged over 50 grid points in the *y* direction. Domain D05 with (a) $\Delta = 30$ m, from $y = 0$ to 24 km every 1.5 km and (b) Δ=8.2 m, from $y = 0$ to 6560 m every 410 m. The colors from blue to red on n jet color scale indicate distance from the southern boundary of the domain.

reduced from the original 24,750 m × 24,750 m to 6750 m × 6750 m. This domain size is enough for the relatively flat topography of the surrounding area, and is several times larger than the domain sizes utilized to simulate stable ABLs in idealized LES setups, which are commonly less than 1 km [e.g., *Kosović and Curry*, 2000; *Beare et al*., 2006; *Zhou and Chow*, 2011]. However, caution must be taken in the presence of complex terrain topography, as recent studies show that mesoscale one-dimensional PBL schemes fail to correctly reproduce the interaction between large-scale stratified flows and terrain [*Muñoz-Esparza et al*., 2016], and the LES domain should encompass the relevant topographic features and incorporate resolved turbulence in the ABL [*Sauer et al*., 2016]. The requirements of horizontal grid resolution to properly resolve stably-stratified turbulence together with domain extension in convective conditions precluded the development of the convective ABL to interact with resolved stratified turbulence in our simulations. Nevertheless, the consequence of misrepresenting nighttime ABL turbulence on daytime convection has been shown to be small [*van Stratum and Stevens*, 2015].

5. Multiscale Diurnal Cycle Results: Comparison to Lidar and Surface Observations

This section presents a detailed comparison of the multiscale modeling results to the wind lidar and surface high-frequency measurements of velocity components, temperature and momentum flux. Particular emphasis is made on the adequacy of the multiscale (coupled mesoscale-LES) modeling framework to properly represent turbulent structures and on the improvements with respect to a mesoscale simulation.

Comparisons of the lidar and WRF "virtual" lidar simulations (see Appendix A for details) suggest reasonable agreement. Time-height evolutions of wind speed, wind direction and turbulent kinetic energy, TKE = 0.5 $\sum u_i'$, measured by the lidar and derived from the multiscale WRF simulation appear in Figure 14. For TKE calculations, a 10 min interval was considered to obtain the turbulent fluctuations, after detrending of the signal to remove any mesoscale variability. The time-height evolution of wind speed (Figures 14a and 14b) displays remarkably similar features. During stable conditions, the multiscale WRF simulation correctly reproduces the strong shear associated with the development of a low-level jet (LLJ). However, the details of the pulsation of the LLJ are slightly different. In both cases, a continuous wind speed increase is present during the first 2 h, however, simulated winds become stronger at 0200–0400 UTC (2100–2300 LT) while such intensification occurs at a later time in the observations (0400–0600 UTC, 2300–0100 UTC). A similar

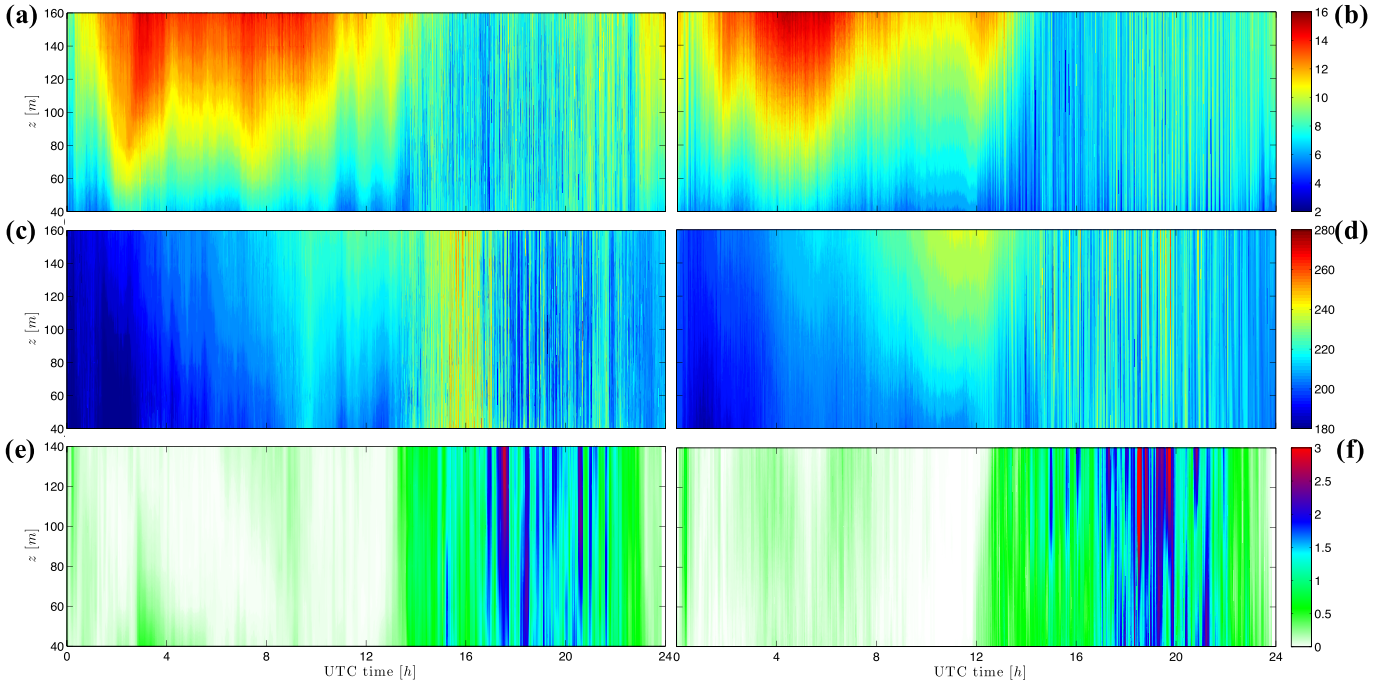

Figure 14. Time-height evolution of (a, b) wind speed (m s^{-1}), (c, d) wind direction (°), and (e, f) turbulent kinetic energy (m^2 s^{-2}), during the 26 August 2013 from the wind lidar (Figures 14a, 14c, and 14e) and the multiscale WRF virtual lidar results (Figures 14b, 14d, and 14f).

effect is found at 08–10 UTC (0300–0500 LT), with the observations in this case revealing weaker wind although vertical wind shear is similar in both cases. Some degree of variation is expected due to the forcings not being perfect, but the structure of the simulated ABL reveals a high degree of fidelity despite the challenges in simulating stable boundary layers [e.g., *Holtslag et al*., 2013]. After 1200 UTC, the multiscale WRF results closely resemble the well-mixed structure of the daytime convective boundary layer. Slightly smoother vertical variability is observed, mostly attributed to scales smaller than the grid size that are not captured by the model. Regarding wind direction, similar features are reproduced by the model results, with a persistent bias of 8° during the entire cycle, arising from the mesoscale forcing (the same bias is present on D03 results). Also, the direction of the simulated ABL (Figure 14c) is primarily 230°, while the observations (Figure 14d) are more easterly from 1600 to 1800 UTC (1100–1300 LT). To a significant degree, the observed structure and magnitude of turbulence are accurately captured by the simulations. The nighttime period is characterized by low turbulence levels, with occasional episodes of turbulence bursts [*Ohya et al*., 2008], with a clear example observed on TKE at $z = 40$ m (Figure 14e) from 0300 UTC (2200 LT) to 0400 UTC (2300 LT). Increased TKE levels start to appear with the onset of convective instability. The multiscale results (Figure 14f) reveal a slightly premature increase of turbulence at 1200 UTC (0700 LT), which does not show up in the observations until 1300 UTC (0800 LT). Afterward, the simulation accurately captures both the amplitude and the timing of the progressive growth and reduction of TKE. As for the stable part of the cycle, the structure of the ABL is accurately reproduced.

Time series at specific levels illustrate the advantage of the nested WRF-LES simulations in capturing the variability of horizontal wind speed, vertical velocity, and TKE at $z = 40$ and 140 m (Figure 15). For the sake of consistency, mesoscale results from domain D03 ($\Delta = 990$ m) were included and postprocessed applying the same range weighting function (RWF) as for the lidar and multiscale WRF simulation (mesoscale simulation otherwise produces homogenous fields within the lidar measurement cone). This comparison documents the significant improvement of the multiscale modeling over the mesoscale simulation results. The multiscale simulation generates turbulence fluctuations that are in very good agreement with the actual lidar observations during daytime and nighttime conditions, displaying both signals extremely similar features. In particular, a couple of aspects can be inferred from the evolution of vertical velocity that are representative of realistic phenomena reproduced by the multiscale simulations (Figure 15b). During the daytime part of the cycle, the multiscale model reproduces the progressive growth and amplitude of the vertical velocity fluctuations with such accuracy that the signal is nearly indistinguishable from the observations. During the nighttime period, vertical velocity at $z = 140$ m exhibits a wave-train-like signal from 0200 to 1000 UTC with two pockets of locally enhanced turbulence (0300, 0600 UTC; 2200, 0100 LT) lasting for approximately 2 h and followed by a strong attenuation (from $|w| = 0.5$ to 0.2 m s^{-1}). This is a signature of global intermittency emerging during stably-stratified conditions [*Mahrt*, 1989] that is also observed by the lidar. In contrast, the mesoscale simulation displays zero vertical velocity in both cases.

Different turbulence regimes can emerge during nighttime stratified conditions in the atmospheric boundary layer. *Van de Wiel et al*. [2003] proposed a classification for stable turbulence regimes based on time-series of surface fluxes during the CASES-99 field experiment. They identified three regimes: continuous turbulence, intermittent turbulence, and radiative cooling regimes. To assess the likelihood that global intermittency occurred during the night of the 26 August 2013 at the CWEX site, sensible heat flux (H_s) and net radiation (Q_{net}) derived from shortwave and longwave incoming/outgoing radiation balance were calculated. The time evolution shown in Figure 16 corresponds to the surface flux station north-west of the WC1 wind lidar (separated ≈1.25 km from it), as the surface station closer to the WC1 lidar did not have radiation measurements available. Observations of H_s reveal an irregular time evolution displaying a range of time scales from a few minutes to larger amplitude variations of about 20–30 W m^{-2} over 1–3 h. Also, Q_{net} presents a regular decreasing trend (in magnitude) within the interval 0230–0700 UTC, which is the result of strong cooling during nighttime. In addition, friction velocity magnitude (see Figure 18b) is predominantly smaller than 0.1–0.15 m s^{-1}, consistent with the values presented in *Van de Wiel et al*. [2003, Table 1]. Inspection of these features agrees reasonably well with the characteristics proposed by *Van de Wiel et al*. [2003], therefore further supporting the likelihood of the observed/modeled vertical velocity wave trains to be associated with global intermittency phenomena.

The multiscale simulations show weaker turbulence fluctuations than observed, but this deviation is likely due to the application of the RWF. For $z = 40$ m, the strength of the velocity fluctuations in the multiscale

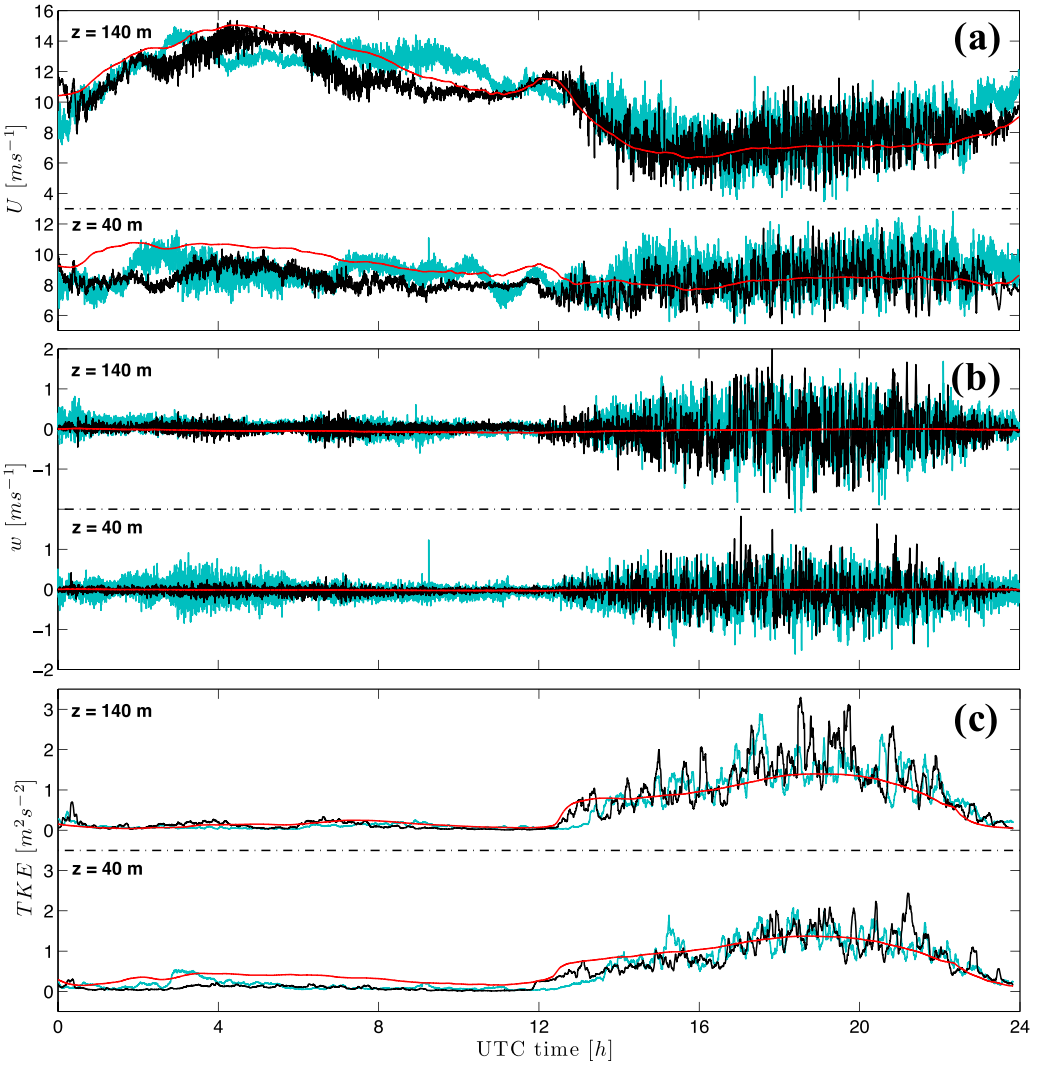

Figure 15. Time evolution of (a) horizontal wind (m s^{-1}), (b) vertical velocity (m s^{-1}), and (c) turbulent kinetic energy (m^2 s^{-2}), at $z = 40$, 140 m during the 26 August 2013. Lidar measurements (light blue), multiscale WRF (black), and mesoscale WRF (red).

simulations is in general weaker than the lidar observations. The lidar measures fluctuations along the line of sight of each beam that are weighted by the RWF as described in Appendix A. The RWF can be interpreted as a filter in the line-of-sight direction, which uses velocity values $\approx \pm 40$ m along the LOS according to equation (A2). Consequently, the wind retrieval at $z = 40$ m is influenced by the variability near the

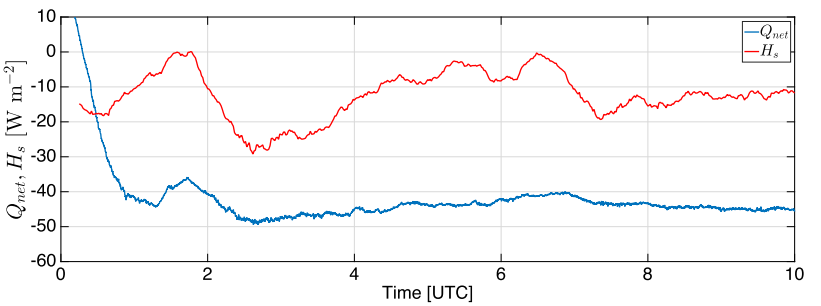

Figure 16. Time evolution of observed sensible heat flux, H_s, and net radiation, Q_{net}, at the surface station located north-west of the WC1 wind lidar during the 26 August 2013 (nighttime period).

surface. In the case of LES modeling, this region is where the SGS component dominates, so the resolved turbulent fluctuations are reduced while in reality turbulence increases as the distance to the surface diminishes. Therefore, it has the effect of partially damping the small-scale variability of the velocity retrieved at $z = 40$ m. This effect is not as evident during convective conditions. Better performance during daytime conditions can be attributed to the nonlocal mixing arising from turbulent transport carried by downdrafts, which are a source of turbulence at the surface that partially compensates for the wall-modeled treatment of the surface layer. Also, production of turbulence during convective conditions occurs at larger scales that are better resolved by the model.

Several aspects of the mean ABL structure were also improved by the multiscale simulation methodology. Interestingly, the temporal evolution of horizontal velocity during nighttime conditions presents intra-hour variability (at temporal scales from a few minutes to an hour) that is not present in the mesoscale results, where variability is only reproduced on a 6 h scale. This points to the fact that small-scale features need to be explicitly resolved in order for the right balance at the larger mesoscales to be achieved. PBL schemes parameterizing the ensemble ABL state cannot provide this small-scale variability. Moreover, the consistent bias of $+1.5$ m s^{-1} of horizontal wind at $z = 40$ m during stable conditions is drastically removed ($+0.4$ m s^{-1}), in turn improving the predicted vertical wind shear by 1.1 s^{-1}. This improvement in the wind speed bias is mainly a consequence of the realistic reduction of the turbulence levels at the near-surface region, which in the case of the mesoscale parameterization are overestimated by 0.3 m^2 s^{-2}. During the core of convective activity (1400–2200 UTC), the mean horizontal wind bias of the mesoscale simulation across the 40–140 m vertical layer, $+2$ m s^{-1}, is again substantially alleviated ($\approx+0.2$ m s^{-1}) in the multiscale simulations. In addition, mean TKE levels at $z = 140$ m from the mesoscale have a positive bias of 0.5 m^2 s^{-2}, which is removed in the multiscale simulations by the improved representation of turbulence from the resolved nested LES domains. In particular, it is worth mentioning that multiscale TKE at 140 m includes instantaneous peaks of $\approx$3 m^2 s^{-2}. These extreme events are relevant for many applications and are not captured by the mesoscale simulation but are accurately reproduced in the multiscale modeling results (both frequency and amplitude).

Further support to this statement is provided by the probability density function (PDF) of horizontal and vertical velocity fluctuations (Figure 17), including the corresponding higher-order moments (skewness, *S*, and kurtosis, *K*). PDFs from the multiscale WRF simulations display a highly similar pattern to those from the lidar observations. In both cases, PDFs during daytime conditions reveal a platykurtic, fat-tail distribution with larger probabilities of extreme turbulent fluctuations ($K_{U'} \approx 0.70$–0.87), with the PDFs from WRF multiscale being almost coincident with the exception of a slightly larger probability for $w' > 1.0$ m s^{-1}. We attribute such strong non-Gaussianty to the presence of anisotropic horizontal convective rolls as identified in the numerical simulation. While the PDFs of velocity fluctuations could be affected by the lidar

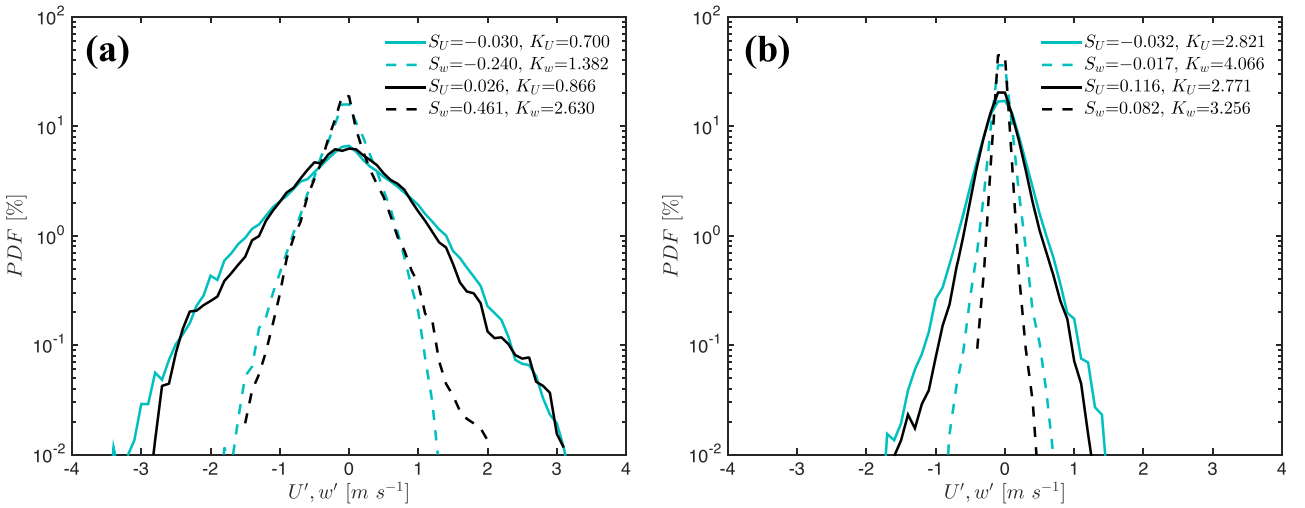

Figure 17. Probability density function of horizontal (solid lines) and vertical (dashed lines) velocity fluctuations during (a) convective and (b) stable conditions. Lidar measurements (light blue) and virtual lidar multiscale WRF (black), over the z = 40–140 m range during the 26 August 2013.

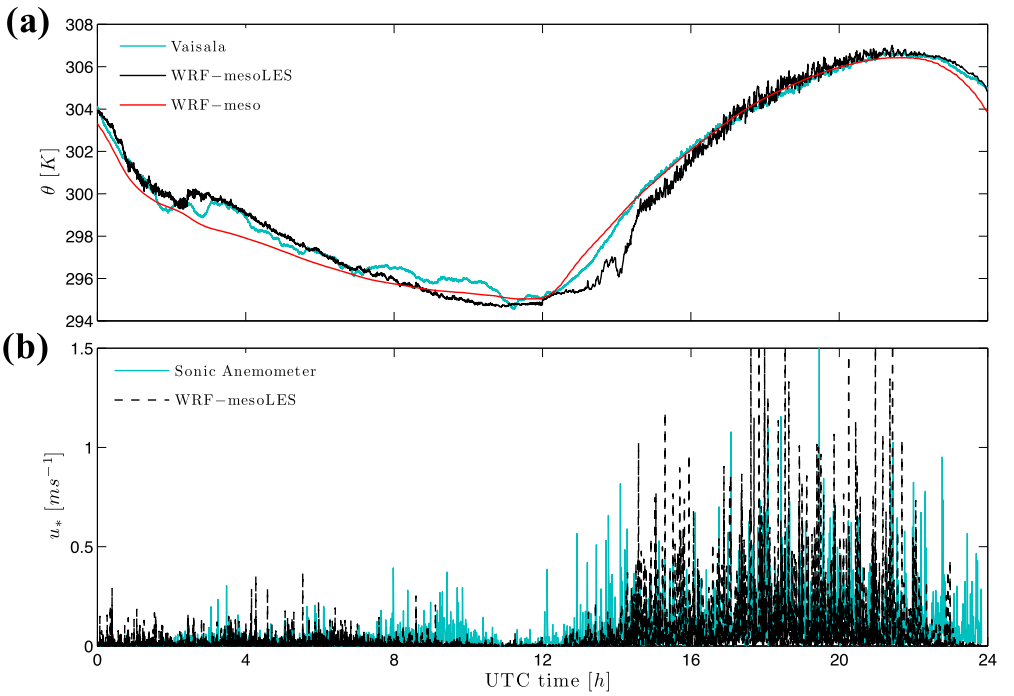

Figure 18. Time evolution of (a) temperature and (b) friction velocity, u_* (m s^{-1}) at $z = 8$ m during the 26 August 2013. Temperature observations are from the HC2S3 Rotronic probe while friction velocity was derived from the 20 Hz 3-D sonic anemometer, both sensors being part of the surface station. Multiscale WRF results correspond to the first vertical grid point.

measurement process, single point values extracted from the multiscale simulations revealed the same patterns (not shown). Multiscale simulations are capable of accurately capturing extreme velocity fluctuations that occur less frequently (0.01–0.1%). During stably-stratified conditions (Figure 17b), PDFs from the multiscale simulations are also in close agreement with the observations, with slightly narrower distributions. In this case, the structure of turbulence is near Gaussian both for the horizontal and vertical velocity fluctuations, with values of kurtosis of $K_{U',W'} \approx 3$. Regarding the skewness of the distributions, no significant deviation from symmetric distributions is found for any of the stabilities ($S_{U',W'} \approx 0$).

Near-surface temperature evolution at $z = 8$ m (Figure 18a) shows an improved prediction of some features compared to the mesoscale simulation. At 0200–0300 UTC, the multiscale simulation is able to reproduce the inflection from the prior ≈2 K h^{-1} cooling rate and closely reproduces the later cooling rate of ≈1 K h^{-1}. This is due to the intra-hour variability that is explicitly accounted for by the inclusion of resolved turbulence, with such particular inflection being associated with an enhancement of horizontal wind and vertical shear (see Figure 15), which in turn increases turbulence production as seen in the evolution of friction velocity shown in Figure 18b. Interestingly, that episode of enhanced turbulence occurring at ≈0300 UTC (2200 LT) in the observations, and shifted 30 min early in the simulation, results in a local increase of temperature originated from turbulent mixing of warmer air from above. In contrast, such local increase in temperature was not captured by the mesoscale simulation, which continued cooling at a similar rate until 1100 UTC. From 1200 to 1430 UTC, the multiscale simulation exhibits a cold bias coincident with the initiation of daytime convection. We hypothesize that this effect is due to the grid resolution used for the convective period (D05, $\Delta = 30$ m). Such resolution may not be enough to properly resolve small turbulent scales at the early stages of the convective period (1200–1300 UTC, 0700–0800 LT), resulting in the formation of large coherent eddies that will overmix the surface and not allow for the appropriate rate of temperature increase. After more vigorous convection initiates, as seen by the increase in friction velocity at 1400 UTC, temperature quickly recovers and closely follows the observed evolution, accurately predicting the timing of the temperature peak and its value ≈306.4 K at 2200 UTC, as well as the later decrease that is overpredicted by the mesoscale simulation. Also, friction velocity during daytime conditions closely follows the variability and intensity reported by the sonic anemometer flux observations.

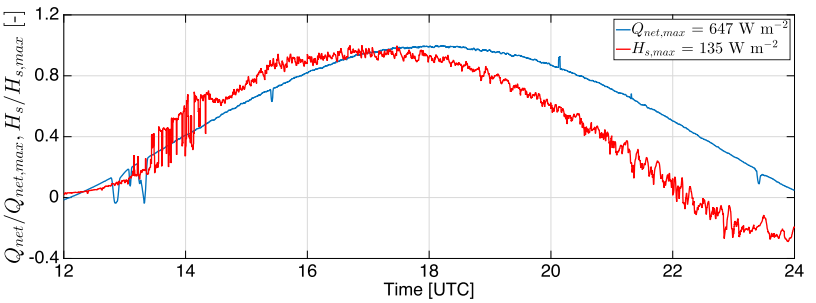

Figure 19. Time evolution of observed net radiation, Q_{net}, at the surface station located north-west of the WC1 wind lidar and simulated sensible heat flux, H_s, from LES domain D05 during the 26 August 2013 (daytime period).

In order to further understand the cold bias of the multiscale simulation during the early-morning hours, time evolution of the surface sensible heat flux, H_s, was analyzed (see Figure 19). In addition, measurements of both shortwave and longwave radiation components from the surface station located north-west of the WC1 wind lidar were used to calculate the net radiation, Q_{net}. For a better appreciation of the variations of H_s and Q_{net}, both signals are divided by their respective maximum values (indicated in the legend). The time evolution of H_s exhibits a highly irregular pattern during 1300–1430 UTC (0800–0930 LT). We hypothesize that such signature is possibly related to the development of small scattered clouds in the multiscale simulation, which would have slowed surface heating and therefore would have contributed to the cold bias. In fact, Q_{net} from the north-west station located 1.25 km from the WC1 wind lidar suggests the presence of clouds in the form of multiple drops from the increasing overall trend. Also, cloud satellite images show numerous small-scale clouds near the CWEX-13 site, further supporting our hypothesis. While these events occurred slightly earlier in reality than in the multiscale simulation, and may not have had the exact same spatial pattern, it is encouraging to see that small-scale clouds can potentially be captured realistically with a multiscale modeling approach such as the one employed herein. Future efforts will focus on analyzing the cloud-ABL interactions with multiscale turbulence-resolving simulations.

Finally, Figure 20 shows a comparison of averaged horizontal velocity energy spectra for stable and convective periods at $z = 8$ m, where the average consists of 1 h subwindows with 75% overlapping (total period is 12 h in both cases). During nighttime conditions, the multiscale simulation exhibits an energy distribution very similar to the sonic anemometer measurements. In both cases, a slope near -1 is present, characteristic of a turbulent production range. For such a close distance to the surface, isotropic turbulence appears at higher frequencies not displayed for a better comparison with modeling results. Energy levels are ≈0.4

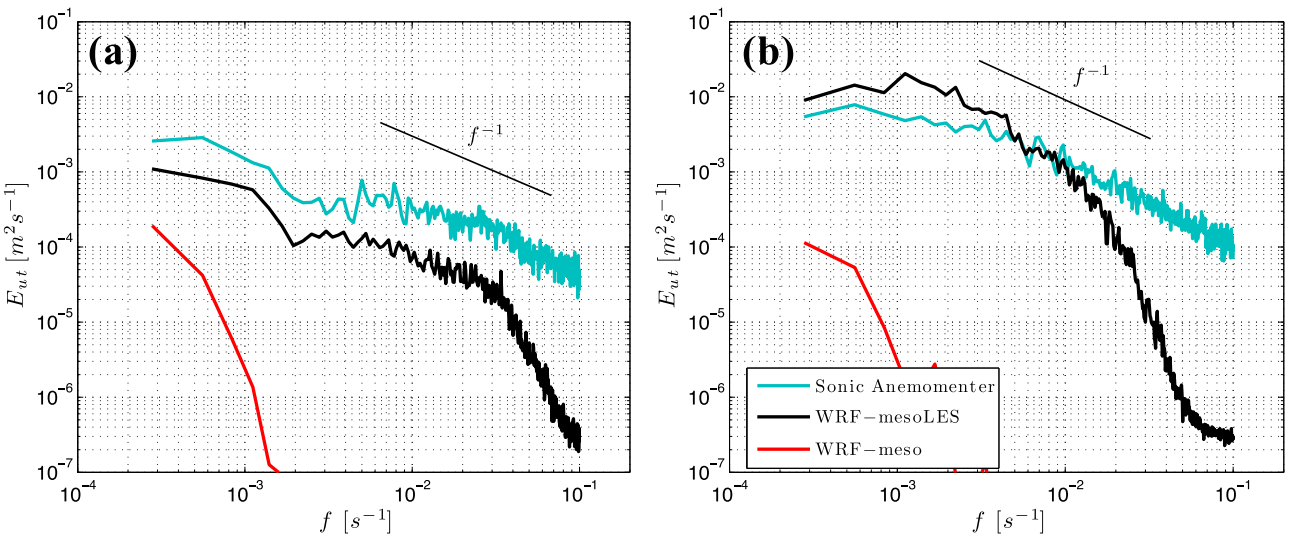

Figure 20. Energy spectra of the horizontal velocity component at $z = 8$ m. Spectra are calculated over 1 h time windows and with a 75% overlapping for the (a) stable and (b) convective periods. Sonic anemometer data was low-pass filtered and decimated to $f = 0.2$ s^{-1} from the 20 s^{-1} raw sampling rate.

times smaller in the multiscale simulations, before numerical dissipation takes place ($f \approx 0.04$ s^{-1}). For the convective part of the cycle, the energy spectrum is also similar to the sonic anemometer observations over the range unaffected by implicit numerical filtering ($0.0003 < f < 0.02$ s^{-1}). In this case, low-frequency energy content is slightly overestimated due to an insufficient energy cascade by resolved small scales. Of course $z = 8$ m corresponds to the first vertical grid point, where the SGS energy represents a significant contribution to the total turbulent energy, and therefore the good agreement in the spectral distribution of turbulent energy can be regarded as a very promising result. Agreement at higher heights is much better and thorough examination of spectra will be reported in a future manuscript.

6. Conclusions

For the first time, dynamical downscaling from synoptic ($\Delta \approx 111,000$ m) down to three-dimensional turbulent eddies in the ABL ($\Delta = 30$, 8.2 m) was performed for a diurnal cycle, and validated using data from the CWEX-13 field experiment. Such disparate-scale modeling presents several challenges carefully addressed herein. The first aspect is to generate resolved turbulence on the LES domains. To that end, we utilized the generalized cell perturbation method [*Muñoz-Esparza et al*., 2014a,] with time-varying perturbation amplitude and height to accommodate the large-scale forcing variations and diurnal evolution. In addition, exponentially decaying perturbations were applied above the boundary layer to incorporate the influence of the residual layer on the growth of the nighttime stable boundary layer.

Our finest grid resolution on the mesoscale domain, $\Delta = 990$ m, resulted in the formation of under-resolved convective structures. We applied an increased c_s coefficient on the two-dimensional Smagorinsky turbulence model for that mesoscale domain to prevent such three-dimensional instability from developing, while maintaining a similar ABL structure. The cell perturbation method largely reduced the fetch to reach a fully developed turbulent state by a factor of 5 with negligible increase in computational burden (a fetch of 45.0 km was required in the unperturbed case). On the contrary, in the presence of under-resolved convection (cell perturbation not applied), the onset of turbulence was further delayed. With a sufficiently large LES domain (75 km $\times$ 75 km), energy spectra exhibited coexistence of a mesoscale energy spectrum with a $-5/3$ slope followed by a three-dimensional production region, -1 slope, and an inertial range with a $-5/3$ slope again. Further nesting of an additional LES revealed that flow equilibration was accelerated for small parent-to-nest grid ratios, and for which a factor of 3 was utilized. In contrast, during nighttime conditions, neither of the two LES domains was able to resolve smaller stably-stratified turbulent eddies ($\Delta = 90$ and 30 m, respectively). To address this issue, an LES domain with a resolution of $\Delta = 8.2$ m was used in place of the $\Delta = 30$ m domain, and upon which the cell perturbation was applied. This increased resolution allowed for a proper production and energy cascade of turbulence to be developed, confirmed by analysis of energy spectra.

Comparison to wind-profiling lidar and near-surface measurements demonstrated the ability to reproduce the ABL structure throughout the entire diurnal cycle with a high degree of fidelity. The multiscale simulations enabled the reproduction of realistic features such as convective rolls and global intermittency, and resulted in PDFs of turbulent velocity fluctuations nearly identical to the lidar measurements. In particular, extreme events were accurately captured both in magnitude and frequency. Moreover, the inclusion of resolved turbulence during nighttime conditions allowed for the right balance between mesoscales and three-dimensional turbulence to be achieved, resulting in intra-hour variability as observed by the lidar and the near-surface temperature sensor, but on the contrary not captured by the mesoscale simulation. Our multiscale simulations improved mean ABL aspects such as reduced horizontal velocities (and reduced TKE levels) and increased vertical shear during nighttime conditions in the near-surface region, and provided bias removal during well-mixed convective hours. Even at the first vertical grid point, where the effect of resolved turbulence is damped by the surface-layer parameterization, energy spectra displayed the same structure as sonic anemometer observations in spite of the slightly lower energy levels in the model results.

This work demonstrates the value of properly performed mesoscale-to-LES coupling to enable multiscale simulations that improve the representation of boundary-layer physics, and has demonstrated that for the resolutions used herein, simulation results closely match the observations by a wind profiler sampling every 5 s. We therefore see multiscale simulations as a powerful tool to gain new insights into real-world ABL phenomenology, to identify parameterization deficiencies and to provide data for validating/developing new

parameterizations. As it has been shown throughout this manuscript, grid resolution is an important factor to these turbulence-resolving simulations. We expect the recently proposed advection scheme from *Kosović et al*. [2016] to allow for a larger range of small scales to be represented and therefore improve the model effective resolution. Also, the use of vertical nesting recently incorporated into WRF should provide more flexibility to set an appropriate grid size for the LES domains [*Daniels et al*., 2016]. For complex terrain topography, a three-dimensional PBL scheme [*Jiménez and Kosović*, 2016] applied within the terra incognita, $\Delta = 150$ m to 1 km, will likely provide better inflow conditions for nested LES in order to further improve the performance of multiscale simulations.

Appendix A: Wind Lidar Retrievals and "Virtual" Lidar Implementation

Lidar wind field retrievals at a given height are a combination of the winds measured along the four beams, and include influence of the LOS velocities through the range weighting function (RWF). Therefore, three-dimensional multiscale WRF results were used to generate a "virtual" lidar so a proper comparison between model and observations can be made. Herein, we followed *Lundquist et al*. [2015] and derived the three-dimensional lidar wind field (u_L, v_L, w_L) by applying the following equations:

$$u_L = \frac{V_{rE} - V_{rW}}{2\sin\psi}, v_L = \frac{V_{rN} - V_{rS}}{2\sin\psi}, w_L = \frac{V_{rN} + V_{rS} + V_{rE} + V_{rW}}{4\cos\psi}. \tag{A1}$$

In the previous expressions, V_{rN}, V_{rS}, V_{rE}, and V_{rW}, are the radial LOS velocities from the north, south, east and west beams, respectively, and ψ is half the cone angle (27.85°). To reflect the actual operating conditions of the lidar, we applied the along-beam RWF of the lidar to the LOS velocities prior to deriving the three-dimensional lidar wind components:

$$\mathrm{RWF}(z) = \frac{1}{c\lambda_m}\left[\mathrm{erf}\left(\frac{4\sqrt{\ln(2)}}{c\lambda}(z - z_0) + \frac{\sqrt{\ln(2)}\lambda_m}{\lambda}\right) - \mathrm{erf}\left(\frac{4\sqrt{\ln(2)}}{c\lambda}(z - z_0) - \frac{\sqrt{\ln(2)}\lambda_m}{\lambda}\right)\right], \tag{A2}$$

where c is the speed of light, λ_m is the range gate (265 ns), λ is the full width half maximum pulse duration (165 ns), and z_0 is the distance along the beam where the measurement is intended to be taken. The wind-profiling lidar performs a sequential scan by each of the four beams with a period of 1.2 s, therefore a cycle is performed in 4.8 s. In the virtual lidar approach, all the beams are sampled simultaneously with a period between consecutive measurements of 5 s. This assumption does not introduce any errors since the effective grid resolution of the simulations does not allow reproduction of atmospheric variability at 1 Hz (as it will be shown later in this section), and therefore the solution remains insignificantly changed within a lidar scanning cycle. Another difference between real and virtual lidars is the fact that, in the numerical simulations, the quality of the backscattered signal is perfect. However, in the case of a real lidar, it does depend on the amount of aerosols carried by the air at a particular location. As mentioned in section 2, a threshold of CNR > -22 dB was applied as a signal quality filter. While this threshold is appropriate for 10 min averages, we found that higher-frequency fluctuations were contaminated at high altitudes where CNR was lower. This effect results in an unphysical enhancement of velocity fluctuations with height. We determined that, for the instantaneous fluctuations, CNR > -16 dB was the limit below which velocity fluctuations systematically increased with height. Application of this more restrictive threshold limited the maximum height of data availability to $z = 160$ m.

Acknowledgments
Part of this research was carried out during DME's postdoctoral appointment at Los Alamos National Laboratory. Most of this work was funded by the A2e Mesoscale-Microscale Coupling project (Department of Energy, Energy Efficiency and Renewable Energy program). Computational resources for this research were provided by the Los Alamos National Laboratory Institutional Computing Program, which is supported by the U.S. Department of Energy National Nuclear Security Administration under contract DE-AC52-06NA25396. We are thankful to the two anonymous reviewers for their appreciation for this work and their interesting insights that have helped to improve the clarity and quality of the manuscript. The authors express great appreciation for the students who helped deploy instrumentation for the CWEX-13 campaign, including Matthew Aitken, Michael Rhodes, Rochelle Worsnop, Clara St. Martin, Ken Tay. We also appreciate the support from the Iowa State team, led by Gene Takle, Russell Doorenbos, Dan Rajewski, and Samantha Irwin, as well as the landowners who enabled the deployment of the instrumentation and the cooperation of the Story County I and II wind farm staff. The authors express appreciation to Nicola Bodini for providing Figure 1. JKL's efforts were supported by the National Science Foundation via grant BCS-1413980 (Coupled Human Natural Systems) and the National Renewable Energy Laboratory under APUP UGA-0-41026-22, the latter supported by the US Department of Energy (Efficiency and Renewable Energy, Wind and Water Power Technologies Office) under contract DE-AC36-08GO28308. The data and model source code used in this paper are available from the corresponding author upon request.

References

Barthelmie, R. J., A. M. Sempreviva, and S. C. Pryor (2010), The influence of humidity fluxes on offshore wind speed profiles, *Ann. Geophys.*, *28*, 1043–1052.

Beare, R. J., et al. (2006), An intercomparison of large-eddy simulations of the stable boundary layer, *Boundary-Layer Meteorol.*, *118*(2), 247–272.

Bingöl, F., J. Mann, and D. Foussekis (2009), Conically scanning lidar error in complex terrain, *Meteorol. Z.*, *18*(2), 189–195.

Blay-Carreras, E., D. Pino, J. Vilà-Guerau de Arellano, A. Van de Boer, O. De Coster, C. Darbieu, O. Hartogensis, F. Lohou, M. Lothon, and H. Pietersen (2014), Role of the residual layer and large-scale subsidence on the development and evolution of the convective boundary layer, *Atmos. Chem. Phys.*, *14*(9), 4515–4530.

Cécé, R., D. Bernard, J. Brioude, and N. Zahibo (2016), Microscale anthropogenic pollution modelling in a small tropical island during weak trade winds: Lagrangian particle dispersion simulations using real nested LES meteorological fields, *Atmos. Environ.*, *139*, 98–112.

Chen, F., and J. Dudhia (2001), Coupling an advanced land surface–hydrology model with the Penn State–NCAR MM5 modeling system. Part I: Model implementation and sensitivity, *Mon. Weather Rev.*, *129*(4), 569–585.

Chen, G., X. Zhu, W. Sha, T. Iwasaki, H. Seko, K. Saito, H. Iwai, and S. Ishii (2015), Toward improved forecasts of sea-breeze horizontal convective rolls at super high resolutions. Part I: Configuration and verification of a Down-Scaling Simulation System (DS3), *Mon. Weather Rev.*, *143*(5), 1849–1872.

Ching, J., R. Rotunno, M. LeMone, A. Martilli, B. Kosović, P. Jiménez, and J. Dudhia (2014), Convectively induced secondary circulations in fine-grid mesoscale numerical weather prediction models, *Mon. Weather Rev.*, *142*(9), 3284–3302.

Chu, X., L. Xue, B. Geerts, R. Rasmussen, and D. Breed (2014), A case study of radar observations and WRF LES simulations of the impact of ground-based glaciogenic seeding on orographic clouds and precipitation. Part I: Observations and model validations, *J. Appl. Meteorol. Climatol.*, *53*(10), 2264–2286.

Daniels, M. H., K. A. Lundquist, J. D. Mirocha, D. J. Wiersema, and F. K. Chow (2016), A new vertical grid nesting capability in the Weather Research and Forecasting (WRF) model, *Mon. Weather Rev.*, *144*(10), 3725–3747.

Dee, D., et al. (2011), The era-interim reanalysis: Configuration and performance of the data assimilation system, *Q. J. R. Meteorol. Soc.*, *137*(656), 553–597.

Dudhia, J. (1989), Numerical study of convection observed during the winter monsoon experiment using a mesoscale two-dimensional model, *J. Atmos. Sci.*, *46*(20), 3077–3107.

Farr, T. G., et al. (2007), The shuttle radar topography mission, *Rev. Geophys.*, *45*, RG2004, doi:10.1029/2005RG000183.

Grossman, R. L. (1982), An analysis of vertical velocity spectra obtained in the bomex fair-weather, trade-wind boundary layer, *Boundary-Layer Meteorol.*, *23*(3), 323–357.

Holtslag, A., et al. (2013), Stable atmospheric boundary-layers and diurnal cycles: Challenges for weather and climate models, *Bull. Am. Meteorol. Soc.*, *94*(11), 1691–1706.

Hong, S.-Y., J. Dudhia, and S.-H. Chen (2004), A revised approach to ice microphysical processes for the bulk parameterization of clouds and precipitation, *Mon. Weather Rev.*, *132*(1), 103–120.

Hong, S.-Y., Y. Noh, and J. Dudhia (2006), A new vertical diffusion package with an explicit treatment of entrainment processes, *Mon. Weather Rev.*, *134*(9), 2318–2341.

Honnert, R., and V. Masson (2014), What is the smallest physically acceptable scale for 1d turbulence schemes?, *Frontiers Earth Sci.*, *2*, 27.

Honnert, R., V. Masson, and F. Couvreux (2011), A diagnostic for evaluating the representation of turbulence in atmospheric models at the kilometric scale, *J. Atmos. Sci.*, *68*(12), 3112–3131.

Ito, J., H. Niino, M. Nakanishi, and C.-H. Moeng (2015), An extension of the Mellor–Yamada model to the terra incognita zone for dry convective mixed layers in the free convection regime, *Boundary-Layer Meteorol.*, *157*(1), 23–43.

Jähn, M., D. Muñoz-Esparza, F. Chouza, O. Reitebuch, O. Knoth, M. Haarig, and A. Ansmann (2016), Investigations of boundary layer structure, cloud characteristics and vertical mixing of aerosols at Barbados with large eddy simulations, *Atmos. Chem. Phys.*, *16*(2), 651–674.

Janjić, Z. I. (1994), The step-mountain eta coordinate model: Further developments of the convection, viscous sublayer, and turbulence closure schemes, *Mon. Weather Rev.*, *122*(5), 927–945.

Jiménez, P., and B. Kosović (2016), Implementation and evaluation of a three dimensional PBL parameterization for simulations of the flow over complex terrain, paper presented at 17th Annual WRF Users' Workshop, National Center for Atmospheric Research, Boulder, Colo.

Jiménez, P. A., J. Dudhia, J. F. González-Rouco, J. Navarro, J. P. Montávez, and E. García-Bustamante (2012), A revised scheme for the WRF surface layer formulation, *Mon. Weather Rev.*, *140*(3), 898–918.

Joe, D. K., H. Zhang, S. P. DeNero, H.-H. Lee, S.-H. Chen, B. C. McDonald, R. A. Harley, and M. J. Kleeman (2014), Implementation of a high-resolution Source-Oriented WRF/Chem model at the Port of Oakland, *Atmos. Environ.*, *82*, 351–363.

Kain, J. S. (2004), The Kain–Fritsch convective parameterization: An update, *J. Appl. Meteorol.*, *43*(1), 170–181.

Kosović, B., and J. A. Curry (2000), A large eddy simulation study of a quasi-steady, stably stratified atmospheric boundary layer, *J. Atmos. Sci.*, *57*, 1052–1068.

Kosović, B., D. Muñoz-Esparza, and J. Sauer (2016), Improving spectral resolution of finite difference schemes for multiscale modeling applications using numerical weather prediction model, paper presented at 22nd Symposium on Boundary Layers and Turbulence, American Meteorological Society, Salt Lake City, Utah.

Lee, G. J., D. Muñoz-Esparza, and C. Yi (2016), Application and validation of cell perturbation method to generate inflow turbulence for large-eddy simulation models in a densely built-up area, in *Proceedings of the Fall Meeting of the Korean Meteorological Society*, pp. 422–424, vol. 10, Korean Meteorological Society, Seoul, South Korea. [Available at http://www.dbpia.co.kr/Article/NODE07049591.]

LeMone, M. A. (1973), The structure and dynamics of horizontal roll vortices in the planetary boundary layer, *J. Atmos. Sci.*, *30*(6), 1077–1091.

Lilly, D. K. (1966), On the application of the eddy viscosity concept in the inertial sub-range of turbulence, *NCAR Manuscr. 123*, 19 pp., Natl. Cent. for Atmos. Res., Boulder, Colo.

Lilly, D. K. (1967), The representation of small scale turbulence in numerical simulation experiments, in *IBM Scientific Computing Symposium on Environmental Sciences*, pp. 195–210.

Liu, Y., T. Warner, Y. Liu, C. Vincent, W. Wu, B. Mahoney, S. Swerdlin, K. Parks, and J. Boehnert (2011), Simultaneous nested modeling from the synoptic scale to the LES scale for wind energy applications, *J. Wind Eng. Ind. Aerodyn.*, *99*(4), 308–319.

Lundquist, J., M. Churchfield, S. Lee, and A. Clifton (2015), Quantifying error of lidar and sodar Doppler beam swinging measurements of wind turbine wakes using computational fluid dynamics, *Atmos. Meas. Tech.*, *8*(2), 907–920.

Lundquist, J. K., et al. (2014), Lidar observations of interacting wind turbine wakes in an onshore wind farm, paper presented at EWEA Meeting Proceedings., European Wind Energy Association, Barcelona, Spain.

Mahrt, L. (1989), Intermittency of atmospheric turbulence, *J. Atmos. Sci.*, *46*(1), 79–95.

Markowski, P. M., and G. H. Bryan (2016), LES of laminar flow in the PBL: A potential problem for convective storm simulations, *Mon. Weather Rev.*, *144*(5), 1841–1850.

Mazzaro, L. J., D. Muñoz-Esparza, J. K. Lundquist, and R. R. Linn (2017), Nested mesoscale-to-LES modeling of the atmospheric boundary layer in the presence of under-resolved convective structures, *J. Adv. Model. Earth Syst.*, *9*, doi:10.1002/2017MS000912.

Mesinger, F., et al. (2006), North American regional reanalysis, *Bull. Am. Meteorol. Soc.*, *87*(3), 343.

Mirocha, J., G. Kirkil, E. Bou-Zeid, F. K. Chow, and B. Kosović (2013), Transition and equilibration of neutral atmospheric boundary layer flow in one-way nested large-eddy simulations using the Weather Research and Forecasting model, *Mon. Weather Rev.*, *141*(3), 918–940.

Mirocha, J., B. Kosović, and G. Kirkil (2014), Resolved turbulence characteristics in large-eddy simulations nested within mesoscale simulations using the Weather Research and Forecasting model, *Mon. Weather Rev.*, *142*(2), 806–831.

Mlawer, E. J., S. J. Taubman, P. D. Brown, M. J. Iacono, and S. A. Clough (1997), Radiative transfer for inhomogeneous atmospheres: RRTM, a validated correlated-k model for the longwave, *J. Geophys. Res.*, *102*(D14), 16,663–16,682.

Monin, A. S., and A. M. Obukhov (1954), Basic turbulent mixing laws in the atmospheric surface layer, *Trudy Geofiz. Inst. Akad. Nauk SSSR*, *24*, 163–187., Tr. Inst. Teor. Geofiz. Akad.

Muñoz-Esparza, D. (2013), Multiscale modelling of atmospheric flows: Towards improving the representation of boundary layer physics, PhD thesis, 188 pp., von Karman Inst. for Fluid Dyn. and Univ. libre de Bruxelles, VKI, Belgium.
Muñoz-Esparza, D., B. Kosović, J. Mirocha, and J. van Beeck (2014a), Bridging the transition from mesoscale to microscale turbulence in numerical weather prediction models, *Boundary-Layer Meteorol.*, *153*(3), 409–440.
Muñoz-Esparza, D., B. Kosović, C. García-Sánchez, and J. van Beeck (2014b), Nesting turbulence in an offshore convective boundary layer using large-eddy simulations, *Boundary-Layer Meteorol.*, *151*(3), 453–478.
Muñoz-Esparza, D., B. Kosović, J. van Beeck, and J. Mirocha (2015), A stochastic perturbation method to generate inflow turbulence in large-eddy simulation models: Application to neutrally stratified atmospheric boundary layers, *Phys. Fluids*, *27*(3), 035102.
Muñoz-Esparza, D., J. A. Sauer, R. R. Linn, and B. Kosović (2016), Limitations of one-dimensional mesoscale PBL parameterizations in reproducing mountain-wave flows, *J. Atmos. Sci.*, *73*, 2603–2614.
Nakanishi, M., and H. Niino (2006), An improved Mellor–Yamada level-3 model: Its numerical stability and application to a regional prediction of advection fog, *Boundary-Layer Meteorol.*, *119*(2), 397–407.
NCEP (2017), *NCEP FNL Operational Model Global Tropospheric Analyses, Continuing From July 1999 (ds083.2)*, doi:10.5065/D6M043C6.
Ohya, Y., R. Nakamura, and T. Uchida (2008), Intermittent bursting of turbulence in a stable boundary layer with low-level jet, *Boundary Layer Meteorol.*, *126*(3), 349–363.
Pope, S. B. (2001), *Turbulent Flows*, IOP Publ., Cambridge University Press, Cambridge, U. K.
Rai, R. K., L. K. Berg, B. Kosović, J. D. Mirocha, M. S. Pekour, and W. J. Shaw (2016), Comparison of measured and numerically simulated turbulence statistics in a convective boundary layer over complex terrain, *Boundary-Layer Meteorol.*, *163*, 69–89.
Rajewski, D. A., et al. (2013), Crop Wind Energy Experiment (CWEX): Observations of surface-layer, boundary layer, and mesoscale interactions with a wind farm, *Bull. Am. Meteorol. Soc.*, *94*(5), 655–672.
Rajewski, D. A., E. S. Takle, J. K. Lundquist, J. H. Prueger, R. L. Pfeiffer, J. L. Hatfield, K. K. Spoth, and R. K. Doorenbos (2014), Changes in fluxes of heat, H_2O, and CO_2 caused by a large wind farm, *Agric. For. Meteorol.*, *194*, 175–187.
Rhodes, M. E., and J. K. Lundquist (2013), The effect of wind-turbine wakes on summertime us midwest atmospheric wind profiles as observed with ground-based Doppler lidar, *Boundary-Layer Meteorol.*, *149*(1), 85–103.
Sauer, J. A., D. Muñoz-Esparza, J. M. Canfield, K. R. Costigan, R. R. Linn, and Y.-J. Kim (2016), A large-eddy simulation study of atmospheric boundary layer influence on stratified flows over terrain, *J. Atmos. Sci.*, *73*, 2615–2632.
Shin, H. H., and S.-Y. Hong (2015), Representation of the subgrid-scale turbulent transport in convective boundary layers at gray-zone resolutions, *Mon. Weather Rev.*, *143*(1), 250–271.
Skamarock, W. C. (2004), Evaluating mesoscale NWP models using kinetic energy spectra, *Mon. Weather Rev.*, *132*(12), 3019–3032.
Skamarock, W. C., and J. B. Klemp (2008), A time-split nonhydrostatic atmospheric model for Weather Research and Forecasting applications, *J. Comput. Phys.*, *227*(7), 3465–3485.
Skamarock, W. C., J. B. Klemp, J. Dudhia, D. O. Gill, D. M. Barker, M. G. Duda, X.-Y. Huang, W. Wang, and J. G. Powers (2008), A description of the Advanced Research WRF version 3, *Tech. Rep. NCAR/TN-475+STR*, NCAR, Boulder, Colo.
Smagorinsky, J. (1963), General circulation experiments with the primitive equations: I. The basic experiment, *Mon. Weather Rev.*, *91*(3), 99–164.
Smagorinsky, J. (1990), Some historical remarks on the use of non-linear viscosities in geophysical models, paper presented at International Conference: Large-Eddy Simulations, Where do We Stand?
Sukoriansky, S., B. Galperin, and V. Perov (2005), Application of a new spectral theory of stably stratified turbulence to the atmospheric boundary layer over sea ice, *Boundary-Layer Meteorol.*, *117*(2), 231–257.
Takle, E. S., D. A. Rajewski, J. K. Lundquist, W. A. Gallus Jr., and A. Sharma (2014), Measurements in support of wind farm simulations and power forecasts: The crop/wind-energy experiments (CWEX), in *Journal of Physics: Conference Series*, vol. *524*, p. 012174, IOP Publ.
Talbot, C., E. Bou-Zeid, and J. Smith (2012), Nested mesoscale large-eddy simulations with WRF: Performance in real test cases, *J. Hydrometeorol.*, *13*(5), 1421–1441.
Van de Wiel, B. J. H., A. F. Moene, O. K. Hartogensis, H. A. R. De Bruin, and A. A. M. Holtslag (2003), Intermittent turbulence in the stable boundary layer over land. Part III: A classification for observations during CASES-99, *J. Atmos. Sci.*, *60*(20), 2509–2522.
van Stratum, B. J., and B. Stevens (2015), The influence of misrepresenting the nocturnal boundary layer on idealized daytime convection in large-eddy simulation, *J. Adv. Model. Earth Syst.*, *7*, 423–436, doi:10.1002/2014MS000370.
Vanderwende, B. J., J. K. Lundquist, M. E. Rhodes, E. S. Takle, and S. L. Irvin (2015), Observing and simulating the summertime low-level jet in central Iowa, *Mon. Weather Rev.*, *143*(6), 2319–2336.
Von Neumann, J., and R. D. Richtmyer (1950), A method for the numerical calculation of hydrodynamic shocks, *J. Appl. Phys.*, *21*(3), 232–237.
Weckwerth, T. M., T. W. Horst, and J. W. Wilson (1999), An observational study of the evolution of horizontal convective rolls, *Mon. Weather Rev.*, *127*(9), 2160–2179.
Wilczak, J. M., S. P. Oncley, and S. A. Stage (2001), Sonic anemometer tilt correction algorithms, *Boundary-Layer Meteorol.*, *99*(1), 127–150.
Wyngaard, J. C. (2004), Toward numerical modeling in the 'terra incognita', *J. Atmos. Sci.*, *61*(14), 1816–1826.
Wyszogrodzki, A. A., S. Miao, and F. Chen (2012), Evaluation of the coupling between mesoscale-WRF and LES-EULAG models for simulating fine-scale urban dispersion, *Atmos. Res.*, *118*, 324–345.
Zhou, B., and F. K. Chow (2011), Large-eddy simulation of the stable boundary layer with explicit filtering and reconstruction turbulence modeling, *J. Atmos. Sci.*, *68*(9), 2142–2155.
Zhou, B., J. S. Simon, and F. K. Chow (2014), The convective boundary layer in the terra incognita, *J. Atmos. Sci.*, *71*(7), 2545–2563.